Volume 47
DOE/DP40200-166

LLE Review

Quarterly Report

April–June 1991

Laboratory for Laser Energetics
College of Engineering and Applied Science
University of Rochester
250 East River Road
Rochester, New York 14623-1299

IN BRIEF

This volume of the LLE Review, covering the period April–June 1991, contains articles on the production and characterization of hot, long-scale-length laser plasmas, a new x-ray spectroscopic method for diagnosing laser-driven target implosions, and two-dimensional (2-D) simulation results that confirm the dominance of kinetic thermal filamentation over ponderomotive filamentation. The section on advanced technology includes a report on the time-domain characterization of bent coplanar waveguides, and a study of the surface disordering of Pb(100) at temperatures below the bulk-melting temperature. Finally, the activities of the National Laser Users Facility and the GDL and OMEGA laser facilities are summarized.

Highlights of the research reported in this issue are

- The production and characterization of hot, long-scale-length laser plasmas provide an opportunity for studying laser-plasma interaction processes that are relevant to reactor-scale targets. Time-delayed subsets of the 24 OMEGA beams have been used to explode small disk targets, producing plasmas with 1-mm scale lengths at densities around eighth critical and whose electron temperatures can be kept at or above 1 keV for extended time periods.
- The observation of a peak in the continuum x-ray spectrum emitted from a laser-imploded target provides a new technique for diagnosing

the compressed shell. The peak is the result of the high absorption of low-energy x rays emitted from the imploding core by the cooler, compressed shell surrounding the core.

- The effects of nonlocal electron heat transport on both thermal and ponderomotive laser filamentation in plasmas have been modeled using a 2-D Fokker-Planck code. These simulations have confirmed recent theoretical predictions that the kinetic thermal mechanism should dominate over the ponderomotive one.
- The time-domain, electro-optic characterization of bent coplanar waveguides has demonstrated that picosecond transients with bandwidth ≥100 GHz can propagate over a large number of bends with limited signal distortion. It is shown that smoothing of the bends considerably improves the very-high-frequency performance of the bent coplanar waveguide.
- Angle-resolved, x-ray photoelectron diffraction studies of the Pb(100) surface have measured the onset of surface disordering (or surface melting) at temperatures below the bulk-melting temperature (600.7 K). It is estimated that the disordered-layer thickness is 4–5 monolayers at 599 K.

CONTENTS

Barukh Yaakobi, Senior Scientist, is shown examining x-ray spectroscopic data obtained from OMEGA target shots. Such data help to analyze and understand the behavior and performance of laser-irradiated targets.

Section 1
PROGRESS IN LASER FUSION

1.A Production and Characterization of Hot, Long-Scale-Length Laser Plasmas

The production and characterization of long-scale-length laser plasmas are essential for the study of the laser-plasma interaction processes that are likely to occur in laser-fusion reactor targets. To carry out such experiments under true reactor conditions, i.e., in spherical geometry for direct-drive laser fusion, would require very large laser energies (comparable to reactor energies) that are presently unavailable. Research has therefore been concentrated on planar targets, with the goal of producing plasmas with scale lengths and electron temperatures as close as possible to those of reactor plasmas.

An extensive series of long-scale-length plasma experiments has been carried out on OMEGA. Thin plastic disks of finite diameter (600 μm) have been exploded using most of the 24 OMEGA beams to form plasmas with scale lengths close to 1 mm. By delaying in time some of the laser beams, electron temperatures $\gtrsim$1 keV have been produced in plasmas of density around eighth critical and maintained over extended periods of time ($\gtrsim$1 ns). This article describes the characterization of these plasmas by a variety of techniques, and shows that the two-dimensional (2-D) plasma expansion and the temporal evolution of the electron temperature and density are in close agreement with *SAGE* simulations. The plasma thus produced forms an excellent tool for investigating laser-plasma interaction processes under conditions relevant to future laser-fusion reactor targets.

Early long-scale-length plasma experiments were carried out using solid targets, with one or more laser beams overlapped onto a large spot of diameter up to 1 mm.[1] The density scale length achieved in this geometry, characterized simply as $L_n = n_e/|\nabla n_e|$ where n_e is the electron density, initially increases with time during the laser pulse, but is eventually limited to some number of order unity times the beam diameter when an initially planar plasma flow develops into a divergent flow; laser energy delivered after this transition is relatively ineffective at increasing the plasma scale length. In the design of these experiments, the fundamental limitation is the available laser energy. If the beam diameter is to be increased with the laser intensity maintained constant, the laser power must be increased in proportion to the beam area; also, the laser duration must be increased, roughly in proportion to the beam diameter, since it will take longer to establish the greater scale length. The energy required thus scales as the cube of the beam diameter. The alternative of reducing the laser intensity while the beam diameter and pulse width are increased would lead to plasmas with unacceptably low electron temperatures ($<<1$ keV) for interaction-physics experiments relevant to reactor plasmas.

Some improvement is available through replacing the solid target by a thin-foil target, which is exploded as a result of irradiation from one or both sides.[2–4] Here, after the laser beam(s) burn through the target, a density profile is obtained that has a maximum in the center. The density scale length L_n as previously defined is infinite in the center, and can be made as large as desired by looking sufficiently close to the center. However, many convective processes (such as filamentation) require that the laser propagate through a significant length of plasma, and for a reasonable comparison to be made with (thick) solid targets it is conventional to define the scale length of the exploding-foil plasma L_p as the FWHM of the density profile, usually measured along the initial target normal. The density profile of an exploding foil differs from that of a direct-drive reactor target in that it has a density maximum but no critical surface at times of interest; however, its characteristics are otherwise generally considered to be sufficiently close to those of reactor plasmas to be of interest. As with the solid target, the scale length of the thin-foil target is limited by the beam diameter for the same reason of divergent flow. However, since the foil expands in both directions, a larger scale length for a given beam diameter might be expected using a foil.

All of the experiments cited so far suffer from a disadvantage that the laser beams serve the dual purposes of forming and interacting with the plasma. They are defocused to a large spot diameter to form the plasma, and so the desired intensities for studying nonlinear laser-plasma interactions (typically up to a few times 10^{15} W/cm^2) may not be available. Additionally, systematic experimentation is difficult since changing the laser intensity desired for a particular interaction-physics experiment will simultaneously change the plasma conditions. This problem has been mitigated by making appropriate adjustments to the laser-beam diameter and pulse width in order to produce a plasma of approximately constant hydrodynamic conditions over a broad range of laser intensities.[3,4] However, an alternate solution is

often preferred. This involves first irradiating a target with a low-intensity, large-diameter plasma-generation beam and then, after the plasma has expanded sufficiently to reach the appropriate density, irradiating the preformed plasma with a high-intensity, tightly focused interaction beam. This technique was first employed using solid targets[5] and has subsequently been used almost exclusively with exploding foils. These latter experiments have been carried out in two distinct geometries: cylindrical[6,7] and line focus.[8] In the first geometry the plasma-generation beam is usually focused to a circular spot with the largest possible diameter, and the interaction beam is incident approximately parallel to the plasma-generation beam. In the second geometry the plasma-generation beam is focused along a line, with the line length equal to the desired scale length, and the interaction beam is incident orthogonally, i.e., along the line focus. This latter geometry has the advantage that a long scale length can be produced with a plasma-generation beam of modest energy; however, the expanded plasma, which is approximately cylindrical about the axis of the interaction beam, is subject to strong transverse density gradients. Alignment of the interaction beam is thus made difficult due to refraction, and the homogeneity of the plasma seen by the interaction beam is harder to ensure.

While many of these experiments have successfully accessed plasma conditions not currently available in spherical geometry, both cylindrical and line-focus geometries suffer from a limited ability to simultaneously achieve the desired plasma density and temperature, often leading to plasma electron temperatures well below 1 keV at the time of the interaction beam. This occurs for at least three reasons: (a) the plasma-generation beam is necessarily defocused to a low intensity; (b) the plasma cools during expansion to the desired density; and (c) as the plasma expands to densities significantly below critical, inverse-bremsstrahlung absorption of laser energy becomes progressively less effective. In spite of this problem, such plasmas do form a useful test-bed for plasma-physics experiments; in particular, they are strongly perturbed by the interaction beam and are subject to strong self-focusing (thermal and/or ponderomotive). However, for greater relevance to reactor plasmas, higher temperatures are required. Additionally, for a clean interaction-physics experiment, it is generally desirable that the interaction beam cause minimal hydrodynamic perturbation to the plasma. One solution to this problem is to use multiple laser pulses for plasma generation and heating, staggered in time; for example, Batha *et al.*[7] irradiated 15-μm-thick CH foils with five NOVA beams at time $t = 0$, followed by four more beams at t = 1.3 ns and one tightly focused interaction beam at t = 2.7 ns, with 1–2 kJ per beam.

In the current experiments the OMEGA laser has been used to produce hot, long-scale-length plasmas that are approximately isothermal at the interaction time. This has been achieved by exploding the foil with a subset of the 24 beams and, after an appropriate time delay, using another subset to maintain the temperature of the expanding plasma. In this respect, the experiment is similar to that of Ref. 7. Furthermore, the choice of a mass-limited target, typically a 6-μm-thick CH foil whose diameter (600 μm) is

matched to the focal diameter of the plasma-generation beams, allows for optical probing of the central region of the plasma, a region that has been obscured by the unirradiated portion of the target in similar experiments using large thin foils. In addition, the plasma created in this way can be nearly spherically symmetric, thus allowing the introduction of the interaction beam from different directions and opening the possibility for conducting experiments with overlapping interaction beams. A further feature of this configuration is that some of the delayed subset of beams can be infrared (1054 nm) in order to provide more efficient heating of the expanding plasma if densities below 10^{21} cm^{-3} (the critical density at 1054 nm) are desired. The OMEGA system also allows for the inclusion of beam-smoothing techniques such as phase plates[9] or smoothing by spectral dispersion (SSD),[10] although most of the results here were obtained without SSD. Typical plasmas produced in the current experiments have center densities around $n_c/8$, and are maintained within a factor of two of this density and at a temperature $T_e \gtrsim 1$ keV for approximately 1 ns, with scale lengths L_p of 0.5–1 mm. (Throughout this article n_c indicates the critical electron density for a laser wavelength of 351 nm, i.e., 9×10^{21} cm^{-3}.)

In this article the experimental conditions and diagnostics are first described in detail. Simulations using the 2-D Eulerian hydrodynamics code *SAGE*[11,12] are discussed in the following section. Experimental results are then presented for the electron temperature measured spectroscopically as a function of time, for the electron density inferred from stimulated Raman scattering (SRS) spectra, and for the 2-D evolution of the plasma as indicated by optical probing. In all cases, it is seen that the experimental results agree well with the predictions of the hydrodynamic simulations. The main conclusion is that these long-scale-length plasmas are well characterized and well suited to interaction-physics experiments of relevance to laser-fusion reactors.

Experimental Conditions and Diagnostics

The target irradiation configuration is shown in Fig. 47.1. Two sets of four opposing beams (P) are used to explode the foil. The on-target laser energy is typically 50–60 J per beam with a pulse duration of ~0.60–0.65 ns at a wavelength of 351 nm. On each side, the four primary plasma-producing beams are surrounded by eight other beams, of which four are used as secondary heating beams, incident 0.6 ns after the primary beams, and three can also irradiate the target as tertiary beams, peaking typically 1 ns after the primary beams. The remaining beam from one side is rerouted to become the interaction beam. Throughout this article the primary beams peak at 1.0 ns, the secondaries at 1.6 ns, and the tertiaries at 2.0 ns. The interaction beam has been located at 1.6 ns in some experiments and at 2.2 ns in others. All beams have a wavelength of 351 nm, except the tertiary beams whose wavelength is 1054 nm.

All primary and secondary beams (but not the tertiary beams) are outfitted with distributed (random) phase plates (DPP's)[9] in front of the focusing lens ($f = 60$ cm) to produce an Airy envelope for the intensity distribution in the

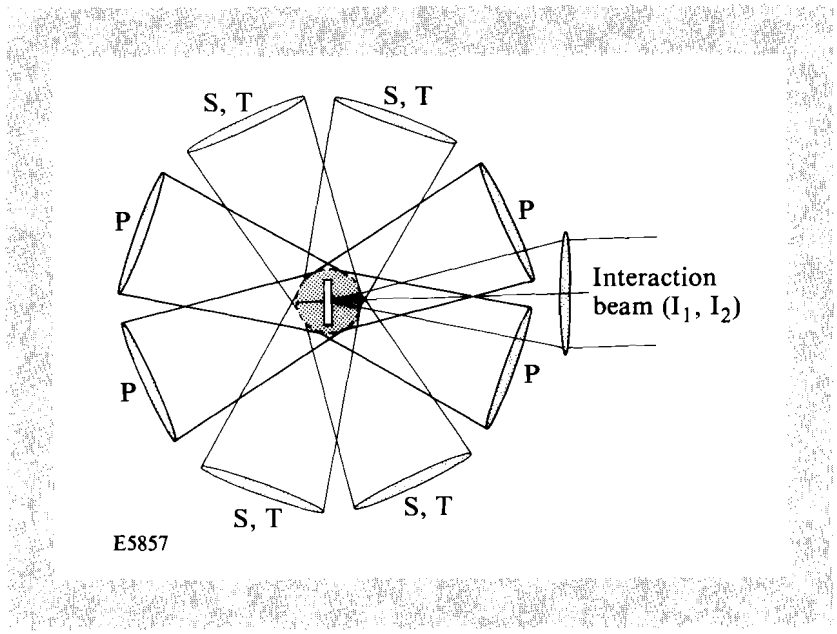

Fig. 47.1
Target irradiation configuration. Schematic layout of 2 × 4 primary plasma-producing beams (P), 2 × 4 secondary (S) and 6 tertiary (T) heating beams, and one interaction beam with two possible timings (I_1, I_2). The interaction beam is tightly focused onto the target (spot diameter ≈ 90-μm FWHM), while all other beams are strongly defocused (spot diameter ≈ 450-μm FWHM). All beams have wavelength 351 nm with ≥60 J/beam on target, except the tertiary beams that have wavelength 1054 nm and ≥100 J/beam. The pulse duration of the UV beams is 600–650 ps.

focal plane of the lens. The 1.25-mm-diam hexagonal cells of the DPP's result in focal spots of ~163-μm FWHM. However, the primary and secondary beams are focused 1.65 mm past the target surface to produce a spot diameter of ~450-μm FWHM. With this focusing, sufficient laser-beam intensity irradiates the edge of the 600-μm-diam target to explode and heat it with a reasonable degree of uniformity, although simulations show the center to expand faster than the edge. The resulting intensities in the primary and secondary heating beams place them below most of the thresholds for nonlinear interaction processes, as has been verified by null experiments without the interaction beam. The wavelength, pulse duration, and energy of the interaction beam are the same as those of the primary beams, but the DPP cell sizes are twice as large (2.5-mm diameter) so that the spot size at best focus is a factor of two smaller. The interaction beam is focused at the center of the target.

Equivalent-target-plane photographs have shown that the envelope of the interaction beam matches well with the predicted Airy envelope $[4J_1^2(x)/x^2]$, which has an FWHM of 82 μm and a radius to the first zero of 97 μm. The Airy envelope is very close to a Gaussian of the same FWHM. The peak (on-axis) intensity of the envelope is found to be $\sim 1.2 \times 10^{15}$ W/cm^2 (for a 60-J beam). The intensity distribution is strongly modulated by the speckle pattern produced by the DPP's, but only ~2% of the beam energy is found to be above 1.5×10^{15} W/cm^2. However, some speckle may be present with a spatial scale of less than the minimum 10 μm that was experimentally resolved.

The primary and secondary beams, which are focused to a plane intermediate between the near field and the far field, are less well characterized, but are approximated by Gaussians of 450-μm FWHM. Diffraction calculations and idealized geometric focusing calculations both suggest an azimuthally

averaged profile with FWHM ≈ 430 μm and an envelope a bit flatter than a Gaussian, assuming a flat distribution of radius 8 cm at the focus lens. As in the case of the interaction beam, a strong speckle pattern is present caused by the DPP's, but the presence of overlapping primary and secondary beams diminishes the high contrast of the speckle pattern to some extent.

After the initial explosion of the foil, thermal conduction is expected to render the plasma density and temperature profiles very smooth by the time the interaction beam is switched on. This process is particularly effective in the presence of the secondary heating beams that help to maintain electron temperatures of greater than 1 keV over nearly 1 ns; in this case speckle in the interaction beam of scale <10 μm should be well smoothed out by thermal conduction.

In all these experiments the targets were free-standing CH foils, 600 μm in diameter and 6 μm thick, mounted on ~10-μm-diam glass stalks. Some targets contained a central Al signature layer of ~1000-Å thickness for x-ray spectroscopy and temperature diagnosis. In addition, all targets were overcoated with 500 Å of Al in order to eliminate or reduce shinethrough effects,[13] i.e., to prevent laser light from penetrating into the target interior prior to plasma formation at the target surface.

The diagnostics employed for these experiments are shown schematically in Fig. 47.2. There were two primary plasma diagnostics, a time-resolved x-ray spectrograph used to determine the electron temperature, and a short

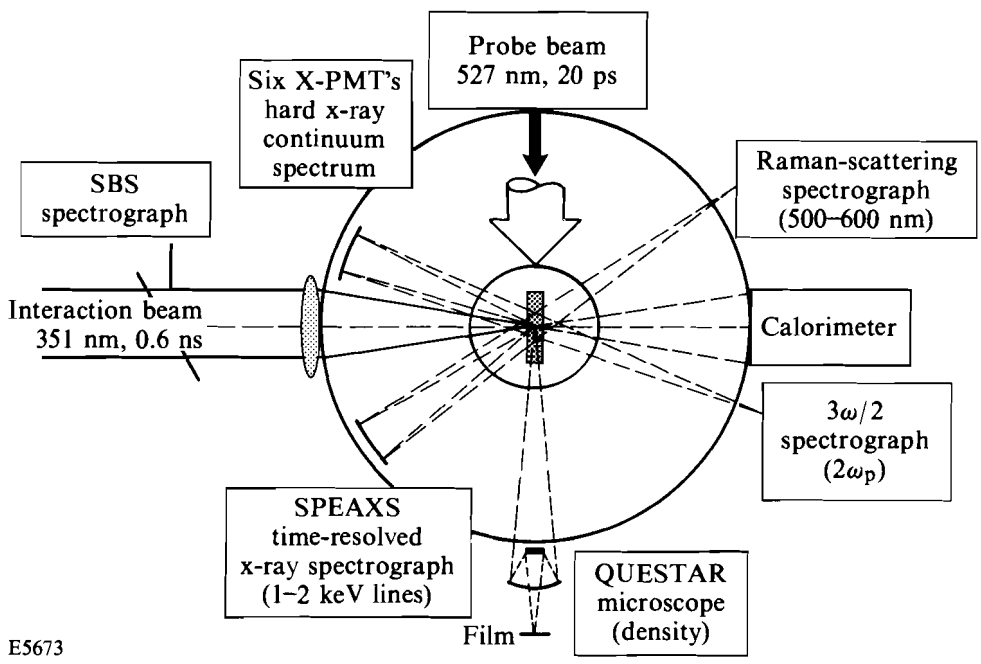

Fig. 47.2
Schematic layout of diagnostics. The polarization of the interaction beam is roughly perpendicular to the plane of the paper; the 3ω/2 collection mirror is actually located above the interaction beam so as to lie approximately within the plane of polarization.

527-nm optical probe beam used in conjunction with a microscope to diagnose the low-density plasma evolution by means of Schlieren photography. In addition, a 1/4-m spectrograph was used to obtain time-integrated visible spectra of the SRS arising from variously timed interaction beams; since SRS is a nonlinear function of laser intensity, this diagnostic provided density measurements in the vicinity of one-tenth critical with some time resolution. The remaining diagnostics were aimed at diagnosing other nonlinear processes such as the two-plasmon decay instability ($3\omega/2$ emission, time-integrated UV spectroscopy), and stimulated Brillouin scattering (SBS, time-integrated UV spectroscopy). Data from these nonlinear processes are presented here only to the extent that they relate to plasma diagnosis. In addition, two channels of K-edge-filtered, hard-x-ray photomultipliers were used for fast-electron diagnostics, and the transmitted light within the original cone of the interaction beam was measured using a calorimeter.

The two-plasmon-decay diagnostic, a 1/4-m spectrograph detecting radiation in the vicinity of $3\omega/2$ (i.e., 234 nm), had its collection mirror in the plane of polarization of the interaction beam (perpendicular to the plane of the drawing), but for ease of graphic representation it is shown otherwise. The stimulated Raman spectra were collected out of the plane of polarization and at ~45° to the interaction beam in the backscatter direction. Both of the SRS and $3\omega/2$ collection optics were $f/8$ spherical mirrors, with either an aluminum coating (for SRS) or a dielectric coating (for $3\omega/2$). Stimulated Brillouin backscattering of the interaction beam was monitored using a diagnostic pick-off with 4% reflection placed in the path of this beam.

The time-resolved x-ray spectroscopy was carried out using the streaked x-ray crystal spectrograph SPEAXS[14] in conjunction with a PET crystal that allowed convenient registration of the Lyβ and Heβ lines of Al with better than 50-ps resolution. A 1000-Å-Al signature layer embedded in the midplane of the target was used to determine the electron temperature evolution using the time-dependent intensity ratio of the Lyβ to the Heβ line. Typical time-resolved spectra are shown in Fig. 47.3 for two cases. In Fig. 47.3(b) the x-ray spectrum is shown for a target without the central Al layer. The outer 500-Å-Al layer is seen to light up early on in the pulse. Doppler splitting in the spectral lines is evident; this occurs because the front and rear sides expand in opposite directions (with velocities ~10^8 cm/s). When a central Al signature layer is employed [Fig. 47.3(a)], strong and long-lasting hydrogen- and helium-like emission is observed. While some Doppler broadening is observed, there is no Doppler splitting from the central Al layer, since this layer always has its highest density (and main emission region) at the center of the plasma where the flow velocity is zero. Figure 47.4 shows intensity-converted line-outs along the time axis for the Lyβ and Heβ lines of Fig. 47.3(a), obtained using the calibration data of Ref. 14.

The temporally varying intensity ratio of the Lyβ and Heβ lines is indicative of the temperature evolution in the plasma. For a given electron density (n_e) and temperature (T_e) this ratio can be calculated using the atomic

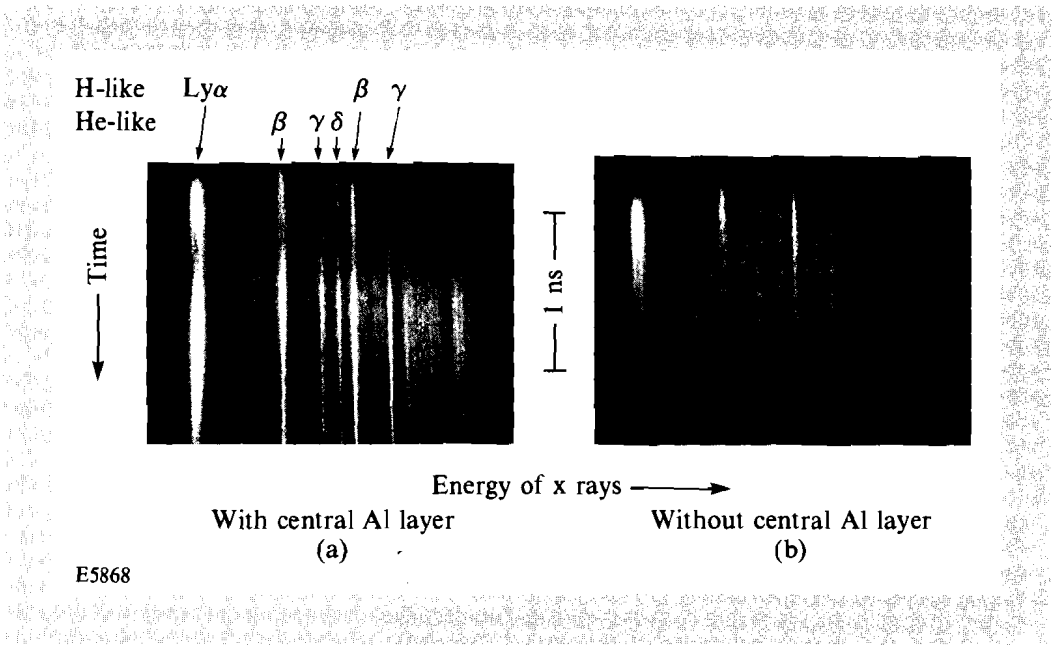

Fig. 47.3
Time-resolved x-ray streak spectra from SPEAXS in the vicinity of the aluminum Heβ and Lyβ lines. (a) 6-μm-thick CH target with a 500-Å-Al barrier layer on each side and a central 1000-Å-Al signature layer; (b) same target but without the signature layer.

rate-equation code POPION.[15] This code uses a detailed-configuration, screened hydrogenic-ion model in a set of multispecies, collisional-radiative rate equations that are solved to obtain the ion species and the required level populations. It is found that the line ratio is only a weak function of n_e; e.g., a factor-of-4 error in n_e typically results in only a ~10% change in the value of T_e corresponding to a given line ratio. Thus, with a reasonable estimate of n_e, the time-dependent electron temperature can be obtained from Fig. 47.4. This method is especially applicable to emission from the center of the target, since the following experimental results support the *SAGE* predictions for the electron density there. However, it is harder to infer the temperature of the outer Al layer at early times since, in this case, the density of the radiating Al is less well known.

The optical probe beam was used to characterize the overall plasma shape and dimension. The choice of a frequency doubled (as opposed to quadrupled) beam resulted in an enhanced sensitivity to low-density regions. The pulse duration was ~20 ps and the synchronization was monitored using fast diodes and a Hewlett-Packard time-interval counter. For some of the experiments a pulse-stacked probe beam was used. This was generated by placing two 70%-reflecting mirrors in the path of the optical probe.

The probe beam was used to take dark-field images of the plasma using light scattered or refracted by the plasma. A 4-in.-diam QUESTAR®[16] model QM1 was used as a microscope with a long working distance (~1 m). The central stop (the secondary mirror of the Cassegrainian telescope) also serves as a beam stop for the dark-field photography. The 2-cm diameter of the beam stop gives a lower cutoff angle corresponding to ~f/50, and the edge of the outer mirror results in an upper cutoff at f/11. For the experiments using the pulse-stacked beam, an enlarged central stop was used whose

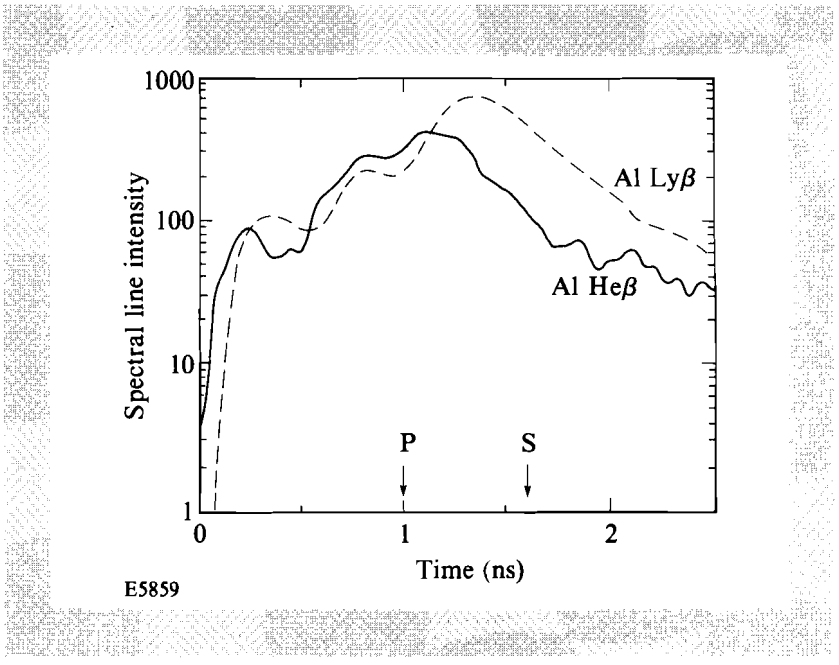

Fig. 47.4
Line-out along the time axis for the Heβ and Lyβ lines for case (a) of Fig. 47.3; P and S indicate the peaks of the primary and secondary beams.

dimensions ($f/14$) differed only slightly from the instrument's entrance aperture. This arrangement resulted in images of only very narrow regions of the plasma, and enabled nonoverlapping multiple exposures of the expanding plasma to be obtained on a single shot, with a precise relative timing, in order to accurately characterize the expansion phase of the plasma.

Two-Dimensional Hydrodynamic Simulations

These experiments have been extensively simulated using *SAGE* in 2-D cylindrical geometry. In order to illustrate the main hydrodynamic features of the formation of typical long-scale-length plasmas, the discussion will focus on a representative simulation with all beams included. The parameters for this simulation, chosen to correspond to one experimental shot discussed below, are summarized in Table 47.I.

The wavelength, pulse width, and timing of the various beams correspond to the standard experimental conditions described in the previous section, with the interaction beam at the later time of 2.2 ns. All UV beams used DPP's and were modeled as spatial Gaussians with the appropriate diameters at half-maximum intensity d_{FWHM}. This is a very good approximation to the ideal Airy profile of the beam envelope. The diameters d_{90} containing 90% of the energy in the Gaussian profile are also given in Table 47.I. Since these diameters correspond to an intensity 10% of the maximum, the 600-μm-diam targets are well irradiated by the primary and secondary beams for which $d_{90} = 820$ μm. For computational efficiency, the spatial profile is truncated at a radius $d_{90}/2$, and the stated energy is delivered within this radius. The peak intensity per beam, defined as the intensity at the peak of the beam in time and at radius $r = 0$, is 3.9×10^{13} W/cm^2 for each of the primary and secondary beams and 9.5×10^{14} W/cm^2 for the interaction beam. Laser-energy deposition is modeled using three-dimensional (3-D) ray tracing.

Table 47.I: Parameters of *SAGE* simulation with all beams included.

	Primary	Secondary	Tertiary	Interaction
Wavelength (nm)	351	351	1054	351
Temporal FWHM (ns)	0.6	0.6	0.6	0.6
Time of peak (ns)	1.0	1.6	2.0	2.2
Number of beams	4/side	4/side	2/side	1 from right
Energy	200 J/side	200 J/side	150 J/side	50 J
Spatial profile	Gaussian	Gaussian	Flat	Gaussian
Diameter d_{FWHM} (μm)	450	450	2000	90
Diameter d_{90} (μm)	820	820	–	160
Peak intensity per beam (W/cm^2)	3.9×10^{13}	3.9×10^{13}	3.3×10^{12}	9.5×10^{14}
Beam geometry	f/0.87 cone	Skew rays at θ_i=69°	Skew rays at θ_i=69°	Parallel beam
Number of rays	15	7 × 4	7 × 4	15
Absorption (%)	77	48	19	40

TC 3011

For computational efficiency, the CH is treated as a fully ionized perfect gas, omitting equation-of-state and radiation effects. For such low-Z material, which is fully ionized at all times except very early in the interaction, this has been found to be a very good approximation. No attempt has been made to model the 1000-Å-Al signature layer in the targets used for spectroscopic diagnostics. This layer, when fully ionized, contains the same number of electrons per unit area as only 0.23 μm of CH (i.e., 4% of the target thickness), and is therefore unlikely to significantly perturb the hydrodynamics. The simulation employs an orthogonal grid, with 40 points up to a radius of 1600 μm and 85 points over 4000 μm in the z direction. The initial target location is at $z = z_{mid} = 2000$ μm.

Results from this simulation are shown at three successive times in Fig. 47.5(a)–(c), corresponding to the peaks of the primary, secondary, and interaction beams. At the time of the peak of the primary beams [Fig. 47.5(a)] the plasma is still overdense and strongly absorbing. Note that only the rays incident from the right are shown, with the ends of the rays marking the 90% absorption point. The outermost rays correspond to the truncation radius of $d_{90}/2$. All four overlapping primary beams are represented as a single beam with a broad $f/0.87$ cone, corresponding to a maximum angle of incidence of 30°. (In the OMEGA geometry, the four beams are each ~$f/3.5$ cones incident at 30.4°.) This representation appears to be reasonable, as refraction is clearly seen to be unimportant (except for the occasional ray that strikes the edge of the target) and there are no problems associated with the

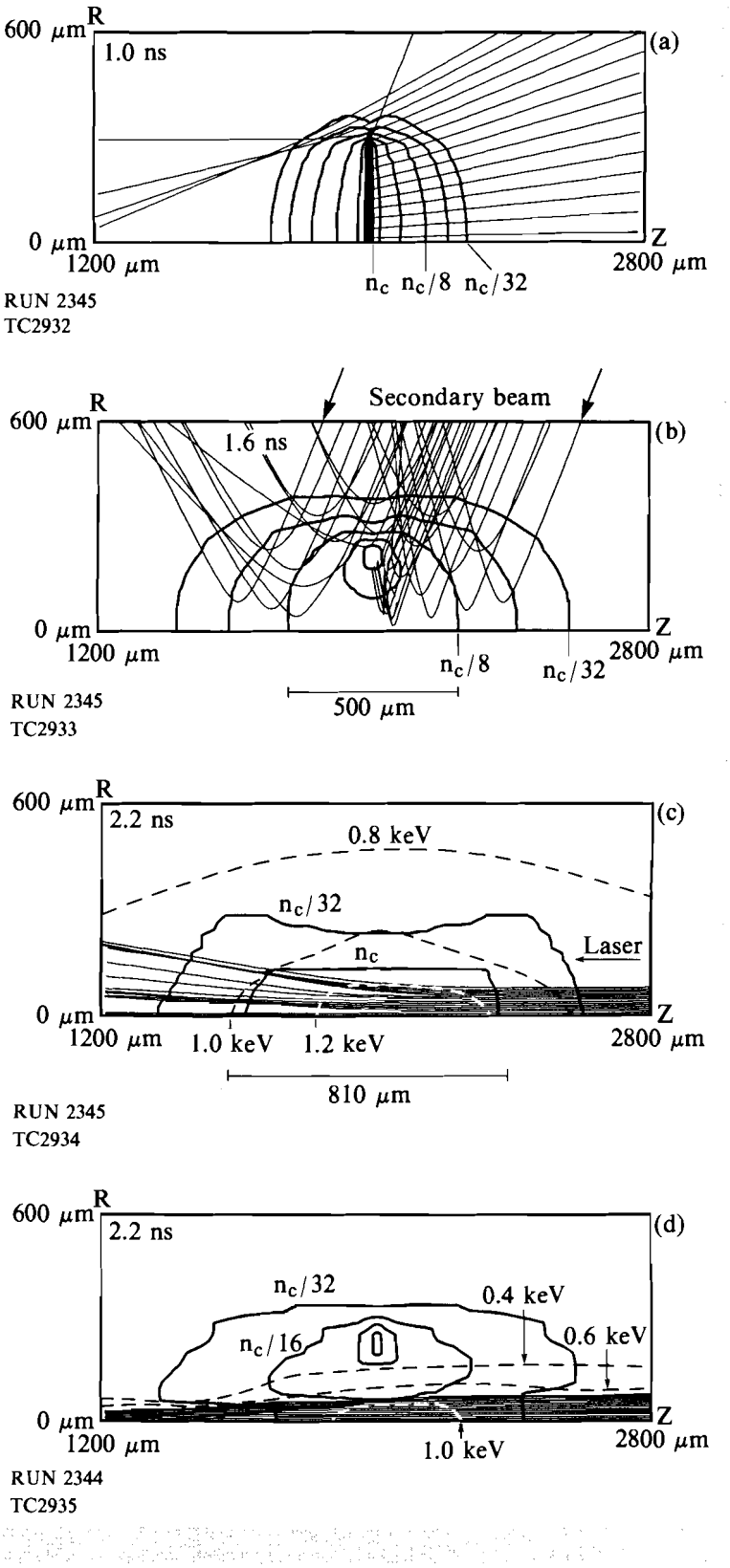

Fig. 47.5
Isodensity contours of the expanding plasma, from a simulation with all beams on, at three successive times: (a) $t = 1.0$ ns, the peak of the primary plasma-producing beams; (b) $t = 1.6$ ns, the peak of the secondary heating beams; and (c) $t = 2.2$ ns, the peak of the interaction beam. In each case typical ray trajectories (from the right side only) are shown for the beam peaking at that time. In case (c), contours of electron temperature are also shown (dashed lines) and indicate a nearly isothermal plasma. The plot shown in (d) is as in (c) but for a different simulation, without the secondary and tertiary beams; here the plasma is significantly perturbed by the interaction beam and high temperatures are found within a long and narrow channel.

geometric foci that lie well beyond the plasma; the main function of the primary beams is to deposit energy on or near the surface of the target. The main shortcoming of this representation is probably the (weakly) 3-D nature of the actual irradiation configuration, where the target-plane irradiation pattern is based on the superposition of two ellipses of aspect ratio cos(30.4°) with their major axes orthogonal. The pattern produced by each set of four primary beams has the same orientation; thus, in the azimuthal direction around the z axis, one should expect to find four regions of somewhat under-irradiated plasma. Just 15 rays per timestep are sufficient to give smooth and convergent plasma behavior. This is made possible by the algorithm whereby *SAGE* deposits ray energy in an area-weighted manner among the four cells nearest each deposition point on the trajectory;[17] thermal diffusion also smooths out residual small-scale deposition nonuniformities.

Figure 47.5(b) shows the corresponding isodensity contours at the peak of the secondary heating beams. The plasma is now underdense and already possesses acceptable characteristics for long-scale-length interaction experiments. Along the axis the peak electron density is $n_e \approx n_c/4$, the electron temperature is $T_e \geq 1$ keV, and the density scale length is $L_p \approx 500$ μm. The density contours show an essentially spherical plasma, well matched to the obliquely incident secondary beams, except for the doughnut-shaped region of high density off axis. This results from the preferential expansion along the axis due to the center-peaked spatial profile of the primary beams. For a while the secondary beams are deflected away from the center of the plasma by this high-density region. It should be noted that the secondary beams are modeled as a cylindrical bundle of parallel rays, incident at 69° to the z axis. Most of these rays thus follow 3-D trajectories that do not lie in the (r,z) plane, and so it is the r and z components of the trajectories that are plotted in Fig. 47.5(b).

At the peak of the interaction beam [Fig. 47.5(c)], the maximum on-axis electron density is one-eighth critical and the scale length $L_p \approx 810$ μm: within this distance, n_e varies between $n_c/8$ and $n_c/16$. It is apparent from the simulation that the interaction beam does not significantly perturb this plasma (this will be quantified later in this article). Furthermore, no evidence of thermal self-focusing is seen, and the plasma deflects the interaction-beam rays outward. This is consistent with the hydrodynamic simulations of Ref. 17 where an example was given of the suppression of thermal self-focusing in a hot, long-scale-length plasma. In Fig. 47.5(c) electron temperature contours are overlaid (dashed lines) and the plasma is seen to be approximately isothermal. Over the whole 810-μm scale length, the interaction beam sees a temperature of 1.0–1.3 keV. The parameters of this plasma should be well suited to interaction-physics experiments.

In order to illustrate the importance of the secondary beams in maintaining a hot plasma, a comparison simulation was carried out with just the primary and interaction beams included. Density and temperature contours for this case are shown in Fig. 47.5(d), at the same time as for Fig. 47.5(c). Here, in

contrast to Fig. 47.5(c), the interaction beam heats a long and narrow cylindrical region in the (moderately) cold preformed plasma, forming a low-density channel that in turn causes the interaction beam to focus (somewhat) to the left of the figure. In broad terms this process may be described as self-focusing, although the region of maximum refraction (near $z = 2000$ μm) is spatially distinct from the focus. In Fig. 47.5(d) the focusing is very weak and not all rays are significantly bent. The locations of the foci vary in time, and a significant increase in the local electron temperature is not seen. The $n_c/32$ contour, however, is somewhat perturbed in the focusing region.

It is evident from Fig. 47.5(c) that the peak temperature and density along the axis are representative of the conditions that the interaction beam sees. By plotting these quantities as a function of time the respective roles of the primary and secondary beams become apparent (Fig. 47.6). The time history of the peak on-axis electron temperature is shown [Fig. 47.6(a)] for four cases ranging from just the primary beams (P) to all beams (P + S + T + I). It is seen that the secondary beams (S) provide substantial plasma heating, and the interaction beam (I) provides some additional heating. On the other hand, the IR tertiary beams (T) clearly provide little heating in this simulation.

One interesting feature of this figure is the delay between the peak of the secondary beams (1.6 ns) and the resulting peak of electron temperature (1.8 ns, for curve P + S). This occurs because, at 1.6 ns, the secondary-beam rays are deflected away from the axis as previously noted in the discussion of Fig. 47.5(b).

The time history of the maximum on-axis electron density for the same four cases [Fig. 47.6(b)] shows a plasma expansion that is at first rapid and then slows down, as has been found in experiments and simulations elsewhere.[3] The main observation here is that the expansion history is determined largely by the primary beams with only minor differences between the four cases. Generally, the density falls faster at late times for the cases where the plasma is heated by extra laser beams, as might be expected. The bump at 2 ns is due to the off-axis doughnut-shaped region of high density "imploding" onto the axis when irradiated by the secondary beams, and does not occur in the case of primary beams only. The exact shape of this bump undoubtedly depends on the symmetry of the irradiation pattern and the resulting off-axis high-density torus. For the small number of beams used in the experiment this symmetry is likely to be far from perfect, as previously discussed, and the bump at 2 ns may actually only be observed as a flat density plateau. In any case, this off-axis region serves as a source of mass that helps maintain the peak on-axis density against what would otherwise be a more rapid decay.

Experimental Results

1. Electron Temperature

One of the distinguishing characteristics of the background plasma formed in these experiments is the extended hot phase of the expanding plasma. This is generally difficult to achieve with laser systems of limited output energy. As is apparent from Fig. 47.6(a), the temporal staggering of

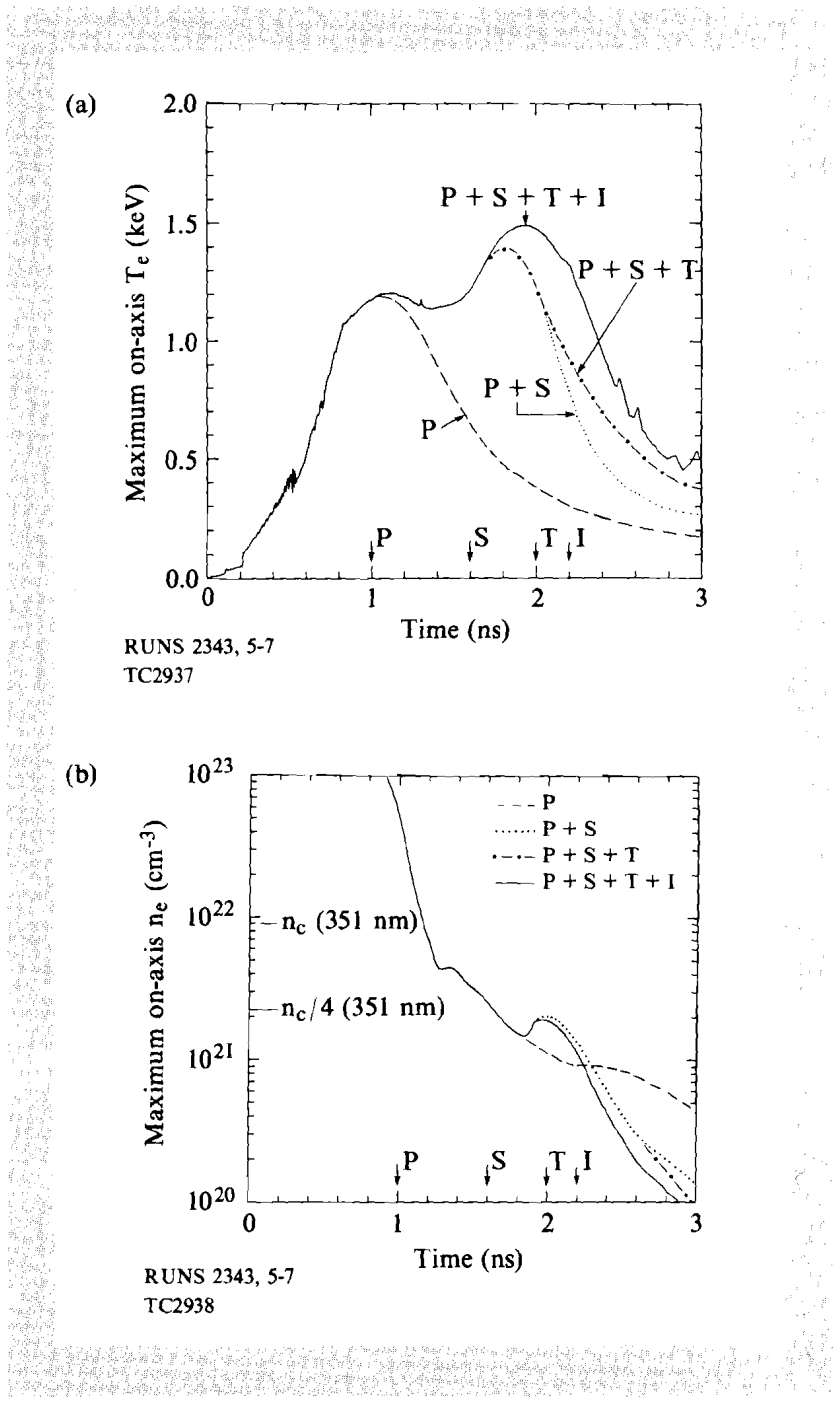

Fig. 47.6
Maximum on-axis electron temperature (a) and density (b) for four cases: (P) primary beams only; (P + S) primary and secondary beams; (P + S + T) primary, secondary and tertiary beams; and (P + S + T + I) all beams.

the various OMEGA beams provides the necessary flexibility. Experimental confirmation has been obtained using targets that included a 1000-Å-Al signature layer in the center of the 6-μm-thick CH disk. Using the temporally resolved x-ray line intensities of the aluminum Lyβ and Heβ lines [Figs. 47.3(a) and 47.4] along with the temperature dependence of the Lyβ to Heβ line ratio calculated by POPION, electron temperatures of 0.8–1.5 keV have been inferred over a period of ~1 ns, as shown in Fig. 47.7. The experimental points in this figure start at ~1 ns because it is at this time that the primary laser

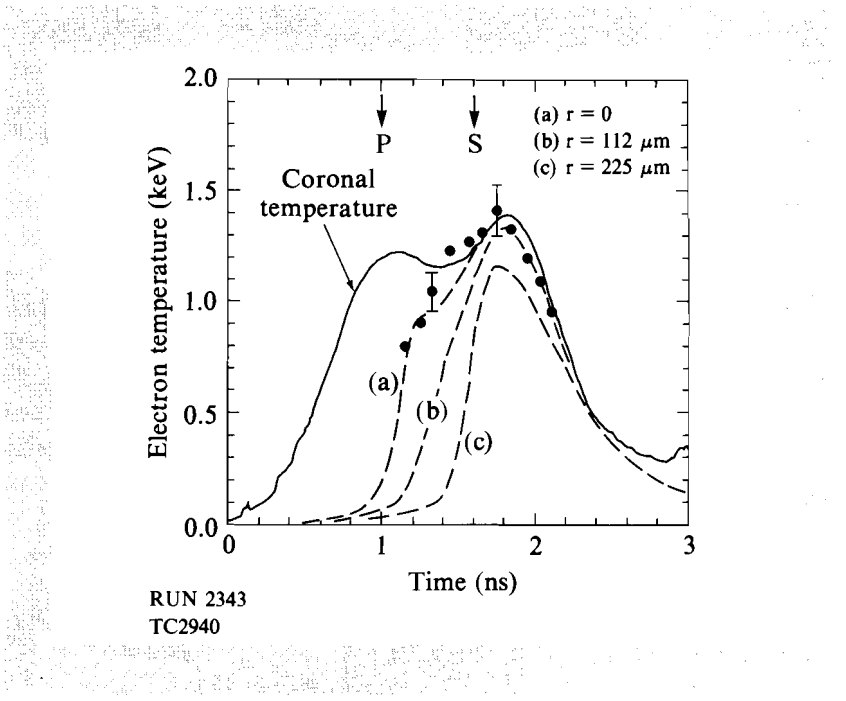

Fig. 47.7
Temporal dependence of the electron temperature as measured by a central 1000-Å-Al layer embedded in the 6-μm-thick CH foil, for a shot with just primary and secondary beams. The experimental points were obtained from the streaked spectra of Fig. 47.3(a) using line ratios calculated by POPION. The solid line indicates two-dimensional *SAGE* predictions for the coronal temperature, defined as the maximum electron temperature along the z axis. The dashed lines indicate predictions for the electron temperature at (a) $r = 0$, (b) $r = 112$ μm, and (c) $r = 225$ μm, at the value of z (z_{mid}) corresponding to the center of the target.

beams have burnt through to the signature layer: at earlier times the line emission is dominated by the 500-Å-thick outer barrier layers, also made of aluminum (see Fig. 47.3).

The dashed curve (a) indicates the electron temperature at the center of the target ($r = 0$) and the solid line the maximum on-axis electron temperature calculated by *SAGE*. The latter temperature is labeled the "coronal" temperature because, early in time, before the primary beams have burnt through to the signature layer, the maximum occurs in the corona rather than at the center of the target. At later times the two calculated temperatures are almost indistinguishable. As expected, the experimental temperatures follow the predicted target-center temperatures early in time. The experimental measurements should correspond to a spatial average over the aluminum in the plasma, and therefore be somewhat lower than on-axis predictions, but this is believed to be a small effect because the plasma is predicted to be fairly close to isothermal. To illustrate this, the dashed curves (b) and (c) give the calculated electron temperature at $r = 112$ μm and at $r = 225$ μm, the latter being the half-maximum radius of the laser-intensity profile; burnthrough at these radii is somewhat delayed with respect to the axis, as expected, but later in time all calculated curves merge. It should be noted that the SPEAXS data did not have an independent timing fiducial for this series of experiments, so that the experimental data was shifted along the time axis to obtain the best fit. The error bars (approximately 10%) shown in this figure are indicative of the error with which the intensity ratio of the two x-ray lines can be determined, as well as the uncertainty in electron density (on which the line ratio is weakly dependent) as previously discussed. The close agreement between simulation and experiment provides evidence that the secondary beams do indeed maintain the plasma temperature.

2. Electron Density via Stimulated Raman Scattering

Stimulated Raman scattering was observed using the 1/4-m spectrograph, but only on shots including the interaction beam. Without the interaction beam there was never any measurable signal except for the near-blackbody plasma background radiation. Typical spectra are shown in Fig. 47.8 for two cases, with the interaction beam timed (a) 0.6 ns and (b) 1.2 ns after the primary plasma-producing beams. In both cases the spectra are narrow. Drake *et al.*[18] reported narrow Raman spectra; their Fig. 4 shows a spectrum taken at 10^{14} W/cm^2 of width 60 nm, and a trend towards broader spectra at higher intensities. In comparison, in case (a) of Fig. 47.8 of this article at 10^{15} W/cm^2, the width is only 27 nm. Although the detailed characteristics of the SRS emission will be discussed in a separate article, it should be pointed out here that the measured SRS threshold corresponds well to the collisional threshold for emission from the center of the parabolic density profile as calculated by Williams[19] for the present conditions.

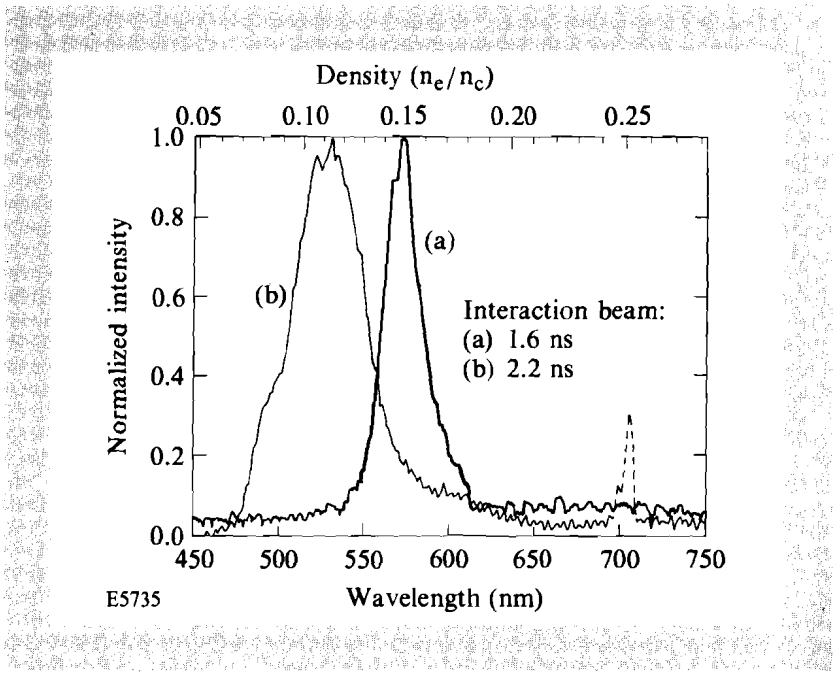

Fig. 47.8
Typical stimulated Raman spectra taken for two cases with different timings of the interaction beam: (a) t = 1.6 ns, the same time as the peak of the secondary heating beams; and (b) t = 2.2 ns. The narrowness of these spectra strongly suggests that the Raman emission originates from the density maximum (along the z axis) and permits an accurate determination of this electron density (top horizontal scale) at the time of the interaction beam.

The narrowness of the SRS spectra, especially in case (a), implies that the emission occurs over a very narrow range of electron densities. The electron density n_e corresponding to an SRS wavelength λ_R is given approximately by the relation $n_e/n_c = (1 - \lambda_0/\lambda_R)^2$, and is shown on the density scale on top of the figure. [Here λ_0 is the laser wavelength, and the very small temperature (Bohm-Gross) correction to the dispersion relation of the plasmons has been neglected.] From Fig. 47.5(b), the electron-density profile around 1.6 ns has a saddle point at the center of the plasma. The instantaneous SRS signal is probably dominated by emission from the saddle-point density, with some width arising from the (small) radial nonuniformity of the density profile. Variations of the saddle-point density over the duration of the interaction beam will add width to the time-integrated spectrum. However, from Fig.

47.6(b), this saddle-point density is stationary just after the peak of the interaction beam, where it has a minimum. It is thus reasonable to expect a very narrow Raman spectrum with wavelength corresponding to the minimum saddle density. This interpretation is supported by the broader spectrum observed at 2.2 ns, where the dominant source density (a true maximum rather than a saddle point) falls monotonically over the duration of the interaction beam.

The two density points obtained from Fig. 47.8 are compared with *SAGE* predictions in Fig. 47.9. Here the heavy solid curve corresponds to the dotted curve of Fig. 47.6(b), for primary and secondary beams only. However, the perturbation of the plasma by the interaction beam, though small, may be significant, and the experimental points should therefore be compared with the dashed curve (interaction beam at 1.6 ns) and the dotted curve (interaction beam at 2.2 ns), respectively. In order to give an indication of the range of densities over which Raman emission is observed, the error bars in Fig. 47.9 denote the densities corresponding to normalized SRS intensities of 0.2 taken from the spectra of Fig. 47.8. In the first case the experimental density point lies very close to the minimum in $n_e(t)$, as expected. In the second case the SRS emission comes predominantly from densities in the range $0.075-0.15\ n_c$, values close to the predicted densities around the time of the interaction beam. In this case it is reasonable to associate the peak of the Raman spectrum with the peak of the interaction beam, since the Raman emission is a strongly nonlinear function of the laser intensity. However, it should be cautioned that the peak of the Raman spectrum does not necessarily give a precise measurement of the peak plasma density at the time of the interaction beam, since Landau damping at lower densities and inverse-

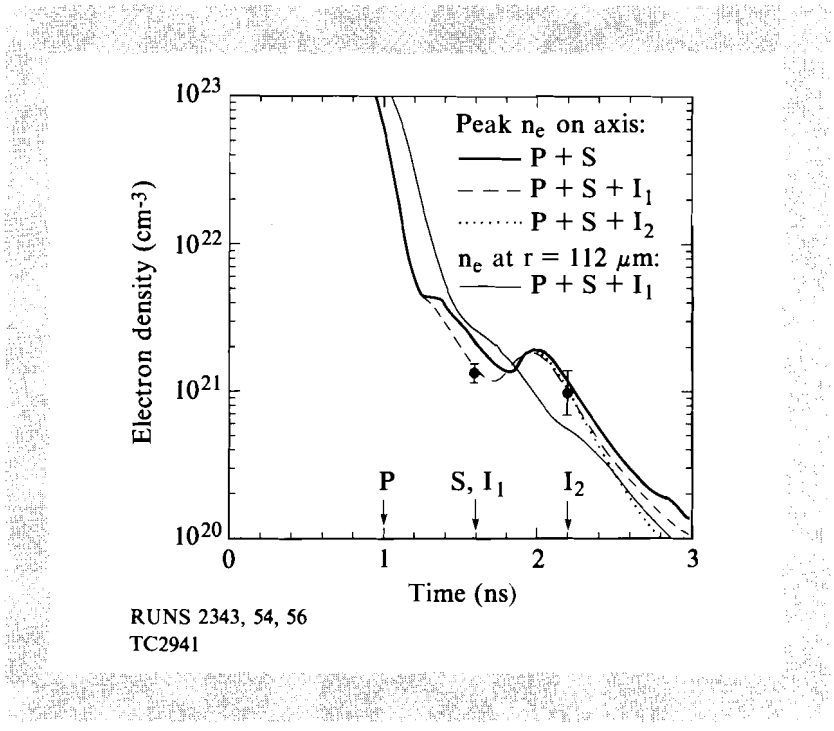

Fig. 47.9
Maximum on-axis electron density as a function of time, as calculated by *SAGE*, for no interaction beam (thick solid curve), for the (50-J) interaction beam located at 1.6 ns (dashed curve), and for the interaction beam at 2.2 ns (dotted curve). The thin solid curve gives the electron density at $r = 112$ μm and $z = z_{mid}$. In all cases the primary (P) and secondary (S) beams are on. Experimental density data, derived from the peaks of the spectra shown in Fig. 47.8, are plotted at the time of the interaction beam. The error bars indicate the density spread corresponding to Raman intensities 20% of the respective maxima in Fig. 47.8. The point at 1.6 ns should be compared with the dashed curve and that at 2.2 ns with the dotted curve.

bremsstrahlung absorption at higher densities could affect the measured spectra.[18] Figure 47.9 also gives the electron density history at a point 112 μm off axis (thin curve); this illustrates that the center of the plasma is a saddle point before 1.8 ns and a maximum thereafter.

In order to examine the extent to which the interaction beam (at 1.6 ns) perturbs the plasma, the density was obtained from Raman spectra such as that of Fig. 47.8 for various interaction-beam energies. The results are plotted in Fig. 47.10, together with *SAGE* predictions obtained from the minima of curves such as the dashed curve of Fig. 47.9. The experimental trend is in good agreement with simulations, and is understood simply on the basis that plasmas that are heated more, expand faster. It is also seen that the perturbation in the plasma density induced by the interaction beam is minimal. On the basis of simulations (compare the solid and dotted curves of Fig. 47.9), even less perturbation of the background plasma is expected when the interaction beam irradiates the lower-density plasma at 2.2 ns.

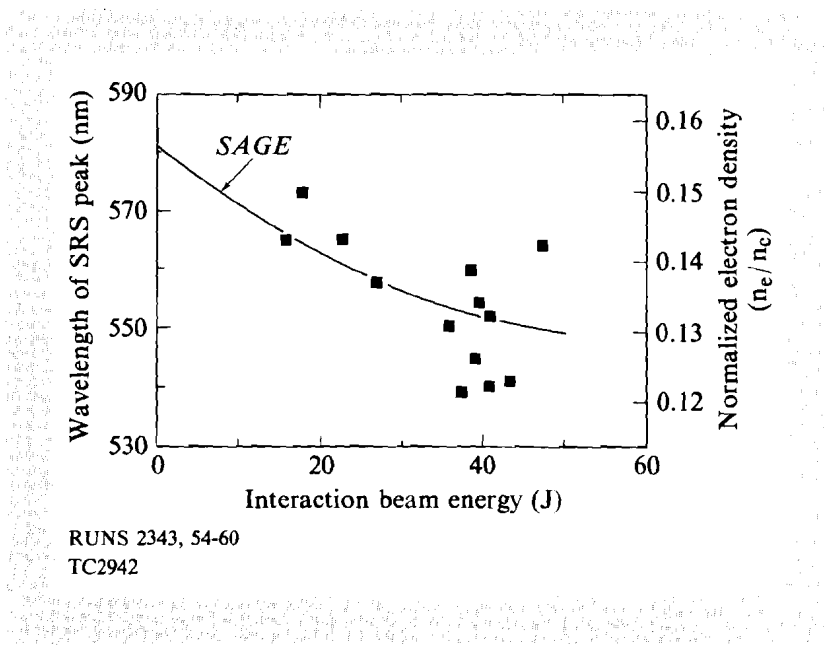

Fig. 47.10
Wavelength of the SRS peak and the corresponding electron density as a function of interaction beam energy on target. In all cases the primary and secondary beams are on and the interaction beam is located at 1.6 ns. The calculated density corresponds to the minimum of curves such as the dashed curve of Fig. 47.9.

3. Electron Density Evolution via Schlieren Photography

The configuration for Schlieren photography used in these experiments is shown schematically in Fig. 47.11. An image of the plasma is produced using just those rays of the probe beam that are bent enough to miss the central circular stop of the QUESTAR (here represented by a simple lens with a central stop) but not so much that they miss the edge of the lens. This straightforward model is incorporated into *TRACER-3*, a 3-D geometric-optics ray-tracing postprocessor to *SAGE*. In practice, diffractive effects can complicate the image, but no attempt has been made to model these effects. *TRACER-3* calculates the trajectories of a 2-D grid of probe rays, typically 30–50 in each dimension, and then generates the boundaries of the Schlieren image simply as contours of equal deflection angle.

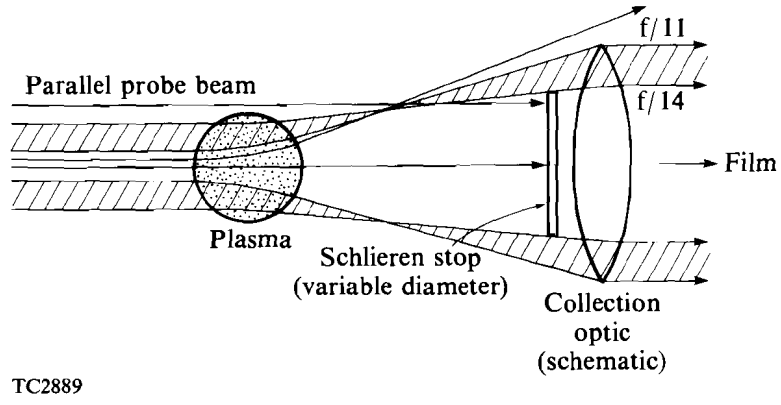

Fig. 47.11
Geometric optics illustration of Schlieren image production using a short-pulse probe beam incident on the target. The size of the primary QUESTAR mirror, represented here by a lens, corresponds to $f/11$. The minimum size of the central Schlieren stop is equal to the diameter of the secondary QUESTAR mirror, corresponding to $f/50$. The central stop was sometimes enlarged to $f/14$ in order to produce narrow images of the expanding plasma for multiple exposures.

Two series of Schlieren photographs were obtained. In the first series, the expansion phase of the plasma was investigated quantitatively by using the pulse-stacked probe beam with an enlarged central stop in front of the QUESTAR microscope. Thus only rays with refraction (or scattering) angles lying in the narrow range between the $f/14$ and $f/11$ focal cones were admitted for image construction. Since the pulses were produced using two 70% mirrors, the energy of each successive pulse was reduced by a factor of two. As a result, the experimental Schlieren pictures only allowed approximately three reasonably distinct exposures. Typical Schlieren images obtained in this way, for three shots with just the primary and secondary beams on, are shown in Fig. 47.12(a)–(c). A problem arises in some of the images because of imperfect centering of the unperturbed (unrefracted) beams on the target and the central aperture stop on the QUESTAR. This, along with a possible slight misalignment of the pulse-stacking mirrors and the steep film-response curve, can easily account for the clearly discernible intensity asymmetries in the images and the apparent loss of portions of some of the rings. However, the originals clearly reveal symmetric structures that can be quantitatively compared with simulations of these images [Fig. 47.12(d)–(f)].

The three Schlieren photographs in Fig. 47.12 were taken with different timings of the probe beam relative to the primary and secondary beams. The relative timings between the primary and secondary beams, and between each probe pulse, are known to high accuracy, but the relative timing between the primary and probe beams (which derive from different oscillators) is less well known. The corresponding times shown in Fig. 47.12 are therefore inferred from the simulations. The simulated images of Fig. 47.12 are reproduced on the same scale as the experimental images, and the close correspondence is easy to demonstrate. The agreement between predictions and experimental observations is indeed very good, giving confidence that the simulations replicate the various plasma parameters with acceptable accuracy.

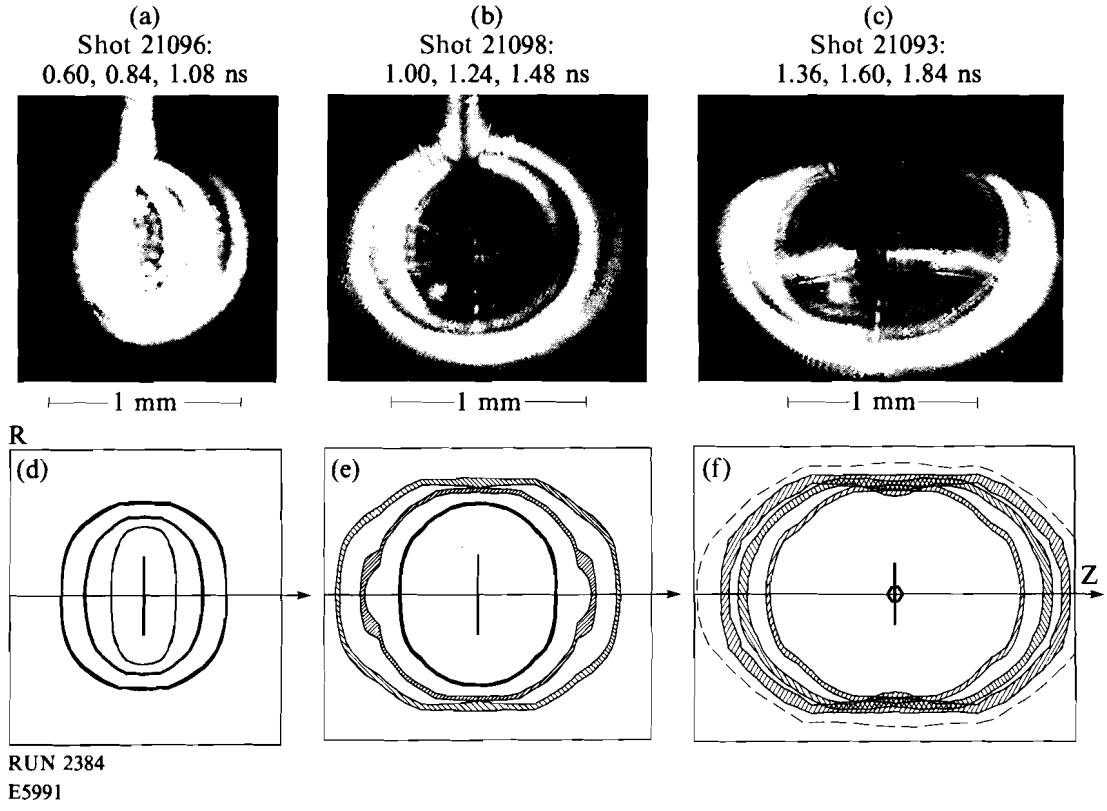

Fig. 47.12
Figures 47.12(a)–47.12(c) show multiple Schlieren images of the expanding plasma, obtained using a ~20-ps, 527-nm probe beam containing a series of pulses of decreasing intensity and separated by 240 ps. In each case the target was irradiated with just the primary and secondary beams. The orientation of the images is consistent with Fig. 47.1, i.e., the horizontal (z) axis is the axis of cylindrical symmetry. A large $f/14$ Schlieren stop was used in conjunction with the $f/11$ collection optics so that each image corresponds to a narrow region of the plasma. The three shots correspond to different timings of the probe beam, ranging from early (a) to late (c). Figures 47.12(d)–47.12(f) show corresponding images predicted by *SAGE* and *TRACER-3*, on the same scale. The dashed curve in (f) is the contour of $n_e/n_c = 0.005$ at the latest time (1.84 ns).

The images of Fig. 47.12 are, of course, contours of deflection angle and not of electron density. However, simulations show that the density contours generally have a similar shape, as illustrated by the dashed curve in Fig. 47.12(f). Thus, the evolution of the Schlieren ring provides a useful visual representation of the evolution of the plasma. Figure 47.12 shows the evolution from an oblate spheroidal plasma shortly after plasma formation, to a spherical plasma, and finally to a prolate spheroidal plasma. Greater expansion along the axial (horizontal) direction than the radial direction is clearly evident.

4. Schlieren Photography in the Presence of the Interaction Beam

A very limited set of experiments was carried out taking Schlieren images

of the plasma in the presence of the interaction beam. For these shots the secondary QUESTAR mirror was employed as the central Schlieren stop, corresponding to $f/50$, and a single probe pulse was used. Figure 47.13 shows two such images, one for the case of no secondary or tertiary heating beams, when the interaction beam was fired into a relatively cold plasma [$T_e \gtrsim 300$ eV, see curve P of Fig. 47.6(a)], and one with all beams on, secondary and tertiary beams included. The interaction beam peaked at 2.2 ns in both cases. The probe beam image was taken at ~2.2–2.4 ns, although, as previously discussed, there is some uncertainty as to the exact relative timing. A comparison of the two cases shows that the hydrodynamic evolution of the plasma in response to the interaction beam is strongly dependent on whether the preformed plasma is hot or cold. The simulated density and temperature profiles at the peak of the interaction beam are shown in Figs. 47.5(c) and 47.5(d).

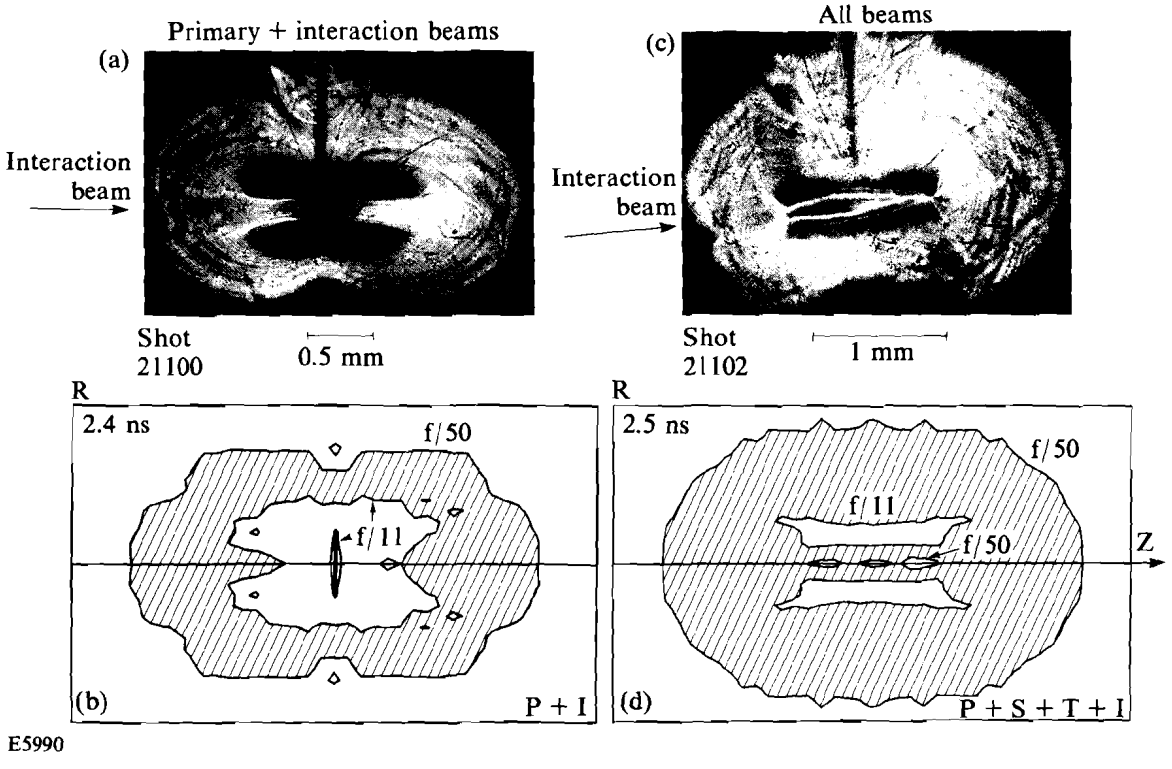

Fig. 47.13
Experimental and simulated Schlieren images of the long-scale-length plasma around the time of the interaction beam (2.2 ns), in 527-nm light deflected between $f/50$ and $f/11$. Left column: primary and interaction beams only; right column: all beams on. Figs. 47.13(b) and 47.13(d) show simulated images at 2.4 ns and 2.5 ns, respectively. In the simulated images, the shaded areas correspond to what would be seen experimentally [bright areas of Figs. 47.13(a) and 47.13(c)]. All images are on the same scale. The interaction beam enters from the left in the experiment, and from the right in the simulations (which are approximately left-right symmetric).

The first image of Fig. 47.13 includes a bright central feature that appears to follow the interaction beam through best focus, where it has the appropriate diameter ($d_{90} = 160$ μm). While it is tempting (and justified to a certain extent) to interpret the image in terms of the interaction beam digging a channel through the preformed plasma, it must be remembered that the Schlieren image gives information about rays that have been deflected (or scattered) a certain amount by the density profile, which in turn has been perturbed in response to the interaction beam. Given that it takes the plasma a finite time to expand after being heated by the interaction beam, the best time to probe may be a little after the peak of the interaction beam.

A simulated Schlieren image for this case is shown in Fig. 47.13(b) at 2.4 ns, the time at which closest correspondence is obtained. The shaded area in the simulated image corresponds to the region between the *f*/50 and *f*/11 contours and should correspond to the bright portions of the experimental image. The size and shape of the outer *f*/50 contour agree well with experiment, consistent with the observations of Fig. 47.12. The central region is obscured by refraction but has almost broken up into two off-axis lobes, subject to strong radial refraction, and most probe rays passing near the z axis are collected. [There is a small region near the center, around the singular ray that passes undeflected through the center of any plasma with exact cylindrical symmetry, where the ray deflection is less than *f*/50, but this region is too small to be significant.] The predicted channel size is, however, somewhat bigger than that observed. It is clear that a series of probe images with precisely known absolute timing would enable an improved understanding to be obtained of the hydrodynamic response of the preformed plasma to the interaction beam.

One feature of the experimental image [Fig. 47.13(a)] that is well explained by the simulations is the break in the channel in the center. This is due to absorption of the probe beam in the cold plasma [<400 eV, see Fig. 47.5(d)] surrounding the channel: at the center of the plasma the probe transmission is calculated to be less than 5%.

The experimental image also shows a number of features not modeled. The outer edge shows a slight left-right asymmetry and a more marked up-down asymmetry, which are caused by a slight misalignment of the probe beam and the QUESTAR optic axes. Since the *f*/50 Schlieren stop, i.e., the secondary mirror of the Cassegrainian optics, subtends a half-angle of 10 mrad, the observed 3–6-mrad alignment error makes a 30%–60% change in the *f* number indicated by the outer edge. There is also a small left-right asymmetry in the intensity of the image (hard to see in the reproduction) most likely due to a small miscentering of the probe beam on the plasma.

The apparent bend in the interaction beam channel (of a few degrees) is probably best explained by imperfect cylindrical symmetry of the plasma that turns the plasma itself into a distorting optical component. Also apparent

in Fig. 47.13(a) is the influence of the stalk that fills out what would otherwise have been a cusp. The cusp, visible in the lower part of this figure, is presumed to be associated with the least-well-irradiated portions around the edge of the target, and is not seen clearly in the simulation, although a cusp-like feature is present in Fig. 47.13(b). This may arise from a lack of adequate spatial resolution in *SAGE* in the vicinity of the edge of the target, but the cusp could reflect the azimuthal asymmetry of the irradiation pattern of the primary beams previously discussed, wherein four regions in the target plane receive less than the average irradiation intensity and expand slower than average. Here it should be noted that the probe beam passes through the target plane at 45° to the axes of the elliptical focal spots; thus two of the under-irradiated regions correspond in location to the top and bottom of the Schlieren image.

The second image [Fig. 47.13(c)] is qualitatively different from the first image. The dark central region is much smaller, almost rectangular in shape, and contains a couple of long, thin, bright regions that cannot reasonably be associated with a beam channel or filaments. A simulation of the Schlieren image at 2.5 ns is shown in Fig. 47.13(d). The outer border again corresponds well with the size and shape of the experimental image. The central feature, however, evolves in a manner consistent with a plasma that is expanding but not significantly perturbed by the interaction beam. (A small perturbation to the experimental image may be seen at the input side.) At 2.2 ns, simulations show that the whole central region is obscured, aside from a small inner area around the singular ray as discussed above. The inner shaded region expands, and by 2.5 ns [Fig. 47.13(d)] has merged with the outer shaded region. This leaves two long, thin, unshaded (i.e., dark) regions off axis where the probe rays are refracted outside the collection optic, and a dark region on the axis (broken up into three islands in the simulation) where rays are not refracted enough to miss the Schlieren stop. All these features are seen at least qualitatively in the experimental image, and quantitatively with respect to their axial extent. In addition, probe-beam transmission through the (hot) plasma is very high, so that no dark central region is either expected or seen in the second experimental image.

Figure 47.13 clearly shows that optical probing can be used to diagnose the significantly different hydrodynamic responses of the plasma to the interaction beam in the two cases. Since the plasma expansion is strongly related to electron thermal transport, particularly in the radial direction, it is also evident that optical-probing diagnostics can potentially provide insight into issues of 2-D thermal transport. *SAGE* uses a standard flux-limited transport model,[17] where the heat flux is directed down the temperature gradient and has a magnitude reduced from the classical Spitzer-Härm[20] value according to a flux limiter[21] f, chosen to be 0.04 for these simulations. The evolution of the preformed plasma in the simulations presented here is in fact rather insensitive to f, since the temperature scale lengths generated are rather long and the heat flow is close to classical; however, steeper temperature gradients are induced in the cold plasma by the tightly focused interaction beam, as seen in Fig. 47.5(d).

It must also be recognized that the flux-limiter model, which has been very successfully used to calculate laser absorption in the coronas surrounding solid targets where both temperature and density gradients are very steep,[12,22] is not necessarily appropriate for the long-scale-length underdense plasmas under consideration here. In addition, recent 2-D Fokker-Planck simulations carried out by Epperlein *et al.*[23] have shown that the heat flux can be reduced below classical in situations where the temperature perturbation scale length is small, even if the temperature gradient scale length ($T_e/|\nabla T_e|$) is long. Such a reduction in heat flux could make thermal self-focusing dominate over ponderomotive self-focusing in many circumstances of interest.[24] At present it is not known experimentally whether the cold plasma is actually as perturbed as *SAGE* predicts [Fig. 47.5(d)], or whether the hot plasma is as unperturbed as predicted [Fig. 47.5(c)], although the experimental data of Fig. 47.10 appears to support *SAGE* predictions for the perturbation to the plasma induced by the 1.6-ns interaction beam. The long-scale-length plasmas produced on OMEGA thus provide a valuable test-bed for studying both 2-D thermal transport and self-focusing.

Conclusion

A novel scheme employing time-staggered beams from the multibeam OMEGA laser system has been used to produce mm-size, long-scale-length plasmas, whose temperatures can be kept at or above 1 keV over an extended period of time during the expansion phase. Such plasmas are of great interest to laser fusion, since they permit many interaction processes to be conveniently studied and they allow the determination of many important parameters such as threshold and saturation intensities. The present scheme has significant advantages of flexibility and the effective use of available laser energy in comparison with some previously used schemes.

These plasmas are formed by a set of 351-nm primary beams focused at near-normal incidence and at low intensity onto thin, 600-μm-diam CH targets, and heated by secondary and tertiary beams focused at oblique incidence. An interaction beam, incident along the initial target normal, is focused at high intensity ($\sim 10^{15}$ W/cm^2) into the preformed plasma and can, with appropriate timing, interact with plasmas of various maximum densities. In these experiments central densities around $n_c/8$ have been accessed at the time of the interaction beam, with the scale length, defined as the FWHM of the density profile, around 0.8 mm.

These plasmas have been diagnosed in three ways. Time-resolved spectroscopic measurements of the ratio of aluminum Lyβ and Heβ lines have indicated electron temperatures in the range 1.0–1.5 keV for a time just under 1 ns. Time-integrated Raman spectra have given a precise diagnosis of the central density around the peak of the interaction beam, and the relative widths of these spectra for different interaction beam timings have indicated different phases in the plasma expansion. The variation with interaction beam energy of the central density obtained from the Raman spectra has provided, probably for the first time, a quantitative measure of the perturbation produced in the plasma by the interaction beam. Finally, Schlieren

imaging of the plasma using a 20-ps, 527-nm probe beam has, through comparison with 2-D hydrodynamic simulations, provided understanding of the 2-D evolution of the plasma.

The characterization of these plasmas is obviously an essential first step toward their use for the study of nonlinear processes. Here the 2-D plasma expansion and the evolution of the electron temperature and density have all been found to be in good agreement with the predictions of the 2-D hydrodynamic code *SAGE*. This agreement permits increased confidence in the predictive capabilities of hydrodynamic codes such as *SAGE* for future experiments.

A number of interaction-physics experiments have been carried out on these plasmas and yielded interesting results. For example, the experimental SRS thresholds are, for the first time, in excellent agreement with analytic theory, within a factor of two, rather than a factor of ~10 below the theoretical predictions as is often found. Also, significantly lower SRS signal intensities are found when smoothing by spectral dispersion (SSD[10]) is implemented on the laser. These results will be reported in detail elsewhere.

Several directions for future work are suggested by the results reported here. Using the beams of the present OMEGA system, and optimizing the focusing and timing of the tertiary beams, it should be possible to extend the range of plasmas accessible to include hotter plasmas and/or plasmas with longer scale lengths and lower densities. By establishing an absolute timing for the short-pulse probe beam, it should be possible to confirm (or constrain) the hydrodynamic modeling of the expansion phase and follow more closely the evolution of the plasma subsequent to irradiation by the interaction beam. This could give insight into the lateral transport of energy deposited by the interaction beam and enable comparison to be made with Fokker-Planck modeling. Finally, by using a 263-nm probe instead of, or in addition to, the 527-nm probe, higher plasma densities will become accessible and it may be possible to study the self-focusing of 351-nm laser light under conditions relevant to laser-fusion reactors.

ACKNOWLEDGMENT

This work was supported by the U.S. Department of Energy Office of Inertial Confinement Fusion under agreement No. DE-FC03-85DP40200 and by the Laser Fusion Feasibility Project at the Laboratory for Laser Energetics, which is sponsored by the New York State Energy Research and Development Authority and the University of Rochester.

REFERENCES

1. D. W. Phillion *et al.*, *Phys. Fluids* **25**, 1434 (1982); E. M. Campbell *et al.*, *Appl. Phys. Lett.* **43**, 54 (1983).
2. D. W. Phillion *et al.*, *Phys. Rev. Lett.* **49**, 1405 (1982); E. M. Campbell *et al.*, in *Laser Interaction and Related Plasma Phenomena*, edited by H. Hora and G. H. Miley (Plenum, NY, 1984), Vol. 6, p. 545; R. E. Turner *et al.*, *Phys. Rev. Lett.* **54**, 189 (1985); R. E. Turner *et al.*, *Phys. Rev. Lett.* **57**, 1725 (1986); J. A. Tarvin *et al.*, *Laser and Particle Beams* **4**, 461 (1986); R. P. Drake *et al.*, *Phys. Fluids B* **1**, 1089 (1989).

3. R. P. Drake *et al.*, *Phys. Fluids* **31**, 1795 (1988).

4. R. P. Drake *et al.*, *Phys. Rev. Lett.* **60**, 1018 (1988); R. P. Drake *et al.*, *Phys. Rev. A* **39**, 3536 (1989).

5. M. J. Herbst *et al.*, *Phys. Rev. Lett.* **52**, 192 (1984); J. A. Stamper *et al.*, *Phys. Fluids* **28**, 2563 (1985); J. H. Gardner *et al.*, *Phys. Fluids* **29**, 1305 (1986).

6. H. Figueroa *et al.*, in *Laser Interaction and Related Plasma Phenomena*, edited by H. Hora and G. H. Miley (Plenum, NY, 1984), Vol. 6, p. 527; H. Figueroa *et al.*, *Phys. Fluids* **27**, 1887 (1984); O. Willi, P. T. Rumsby, and Z. Lin, in *Laser Interaction and Related Plasma Phenomena*, edited by H. Hora and G. H. Miley (Plenum, NY, 1984), Vol. 6, p. 633.

7. S. H. Batha, D. D. Meyerhofer, A. Simon, and R. P. Drake, *Phys. Fluids B* **3**, 448 (1991).

8. O. Willi *et al.*, *Opt. Commun.* **70**, 487 (1989); O. Willi *et al.*, *Phys. Fluids B* **2**, 1318 (1990); C. Labaune *et al.*, in *Laser Interaction with Matter*, edited by G. Verlade, E. Minguez, and J. M. Perlado (World Scientific, Singapore, 1989), p. 185; S. D. Baton, C. Labaune, and J. L. Lacaze, *Opt. Commun.* **74**, 195 (1989).

9. Y. Kato *et al.*, *Phys. Rev. Lett.* **53**, 1057 (1984); LLE Review **33**, 1 (1987).

10. S. Skupsky, R. W. Short, T. Kessler, R. S. Craxton, S. Letzring, and J. M. Soures, *J. Appl. Phys.* **66**, 3456 (1989).

11. R. S. Craxton and R. L. McCrory, LLE Laboratory Report 99, Rochester, NY (1980).

12. R. S. Craxton and R. L. McCrory, LLE Laboratory Report 108, Rochester, NY (1980).

13. J. E. Balmer, T. P. Donaldson, W. Seka, and J. A. Zimmermann, *Opt. Commun.* **24**, 109 (1978); J. Delettrez, D. K. Bradley, P. A. Jaanimagi, and C. P. Verdon, *Phys. Rev. A* **41**, 5583 (1990); D. K. Bradley, T. Boehly, D. L. Brown, J. Delettrez, W. Seka, and D. Smith, in *Laser Interaction and Related Plasma Phenomena*, edited by H. Hora and G. H. Miley (Plenum, NY, 1991), Vol. 9, in press.

14. B. L. Henke and P. A. Jaanimagi, *Rev. Sci. Instrum.* **56**, 1537 (1985).

15. R. Epstein, S. Skupsky, and J. Delettrez, *J. Quant. Spectrosc. Radiat. Transfer* **35**, 131 (1986).

16. QUESTAR Corporation, New Hope, PA 18938.

17. R. S. Craxton and R. L. McCrory, *J. Appl. Phys.* **56**, 108 (1984).

18. R. P. Drake *et al.*, *Phys. Fluids B* **1**, 2217 (1989).

19. E. A. Williams, in *LLNL Laser Program Annual Report 1985*, Lawrence Livermore National Laboratory Report, UCRL 50021-85, pp. 2–46 (1985).

20. L. Spitzer, Jr. and R. Härm, *Phys. Rev.* **89**, 977 (1953).

21. R. C. Malone, R. L. McCrory, and R. L. Morse, *Phys. Rev. Lett.* **34**, 721 (1975).

22. W. Seka, R. S. Craxton, J. Delettrez, L. Goldman, R. Keck, R. L. McCrory, D. Shvarts, J. M. Soures, and R. Boni, *Optics Commun.* **40**, 437 (1982); M. C. Richardson, R. S. Craxton, J. Delettrez, R. L. Keck, R. L. McCrory, W. Seka, and J. M. Soures, *Phys. Rev. Lett.* **54**, 1656 (1985).

23. E. M. Epperlein, G. J. Rickard, and A. R. Bell, *Phys. Rev. Lett.* **61**, 2453 (1988).

24. E. M. Epperlein, *Phys. Rev. Lett.* **65**, 2145 (1990).

1.B Diagnosis of Laser-Compressed Shells Based on Absorption of Core Radiation

A method for diagnosing laser-driven target implosions, particularly of plastic shells, is described. It is based on the fact that most x-ray emission from the core is absorbed by the dense, cooler compressed shell surrounding the core. The core radiation is emitted by the fuel and (mainly) by the inner layer of the compressed shell, and is absorbed by the rest of the compressed shell, which is at a lower temperature. Since the shell is transparent to harder radiation, a peak should be observed in the emerging x-ray spectrum.[1] This peak would shift to higher photon energy as the achieved compression becomes greater. The method is particularly useful for plastic targets (CH), on which we concentrate in this article. This is because in glass shells, as will be shown, the inferred cold-shell $\rho\Delta r$ can be much smaller than the total shell $\rho\Delta r$, reducing the usefulness of the method. Also, fuel-filled plastic targets do not provide line-emission diagnostics, so alternative methods such as this are desirable. It might be thought that the measurement in the case of glass shells is easier because of the greater emission levels as compared to CH targets at the same wavelength. However, the absorption is also much greater in glass, and the position of the peak is reached at higher photon energies, where core emission becomes weaker.

The absorption of x rays in the shell is due to either photoionization (bound-free transitions) in partially ionized material, or inverse bremsstrahlung (free-free transitions) due to the free electrons. In glass-shell targets, the atoms in the cold part of the imploded shell are typically not completely stripped. Therefore, the absorption is predominantly caused by K-shell photoionization, for which the opacity is proportional to the density ($k_{bf} \sim \rho$). In plastic targets, the absorbing shell can be sufficiently hot for the carbon atoms to be highly ionized. For completely stripped ions, the dominant x-ray absorption mechanism is inverse bremsstrahlung, for which the opacity depends on both density and temperature ($k_{ff} \sim \rho^2/T^{1/2}$). The location of the

spectral peak is shown to occur at a wavelength where the optical depth is about 1. Thus, the location of the peak in the emission from glass shells should depend on the shell $\rho\Delta r$ (or more precisely, the integral $\int \rho dr$) of the cold part of the imploded glass shell. In highly ionized plastic-shell material, the position of the peak would be a function of the quantity $\rho^2\Delta r/T^{1/2}$ for the shell. Because of the weak dependence on T, it would effectively be a function of the $\rho^2\Delta r$ (or more precisely, the integral $\int \rho^2 dr$) of the imploded shell.

Since the method relates only to the cold, absorbing part of the shell, we address the question of what fraction of the shell is absorbing. In the case of CH shells, because of the weak dependence of inverse bremsstrahlung absorption on temperature, the hotter, inner layer of the imploded shell can contribute significantly to the total absorption. The cold-shell $\rho^2\Delta r$ value obtained from the position of the peak will thus not be much smaller than that of the total CH shell. On the other hand, the inner, hot layer of an imploded glass shell will have negligible photoionization absorption (because of its atoms being stripped); thus, the $\rho\Delta r$ value derived from the peak will be considerably smaller than that of the total glass shell. This is an additional advantage in applying this method to CH as compared with glass shells.

In general, the importance of inverse bremsstrahlung with respect to photoionization increases with temperature, since the increased ionization reduces the density of ions that can undergo photoionization. In competition with this, the actual opacity based on inverse bremsstrahlung at fixed ionization actually decreases with an increase in the temperature. Inverse bremsstrahlung also becomes more important with an increase in density, for a fixed ionization, because of the different dependences on ρ. However, for a given temperature, the ionization (in LTE) decreases with an increase in the density; this tends to increase the relative importance of photoionization absorption.

Analytical Relations for the Position of the Peak

The opacity due to inverse bremsstrahlung (free-free transitions) is given by[2]

$$k_{ff} = \frac{4\pi Z^2 e^6 g}{3^{3/2} h c m^2 \nu^3} \left\{ \frac{2m}{\pi kT} \right\}^{1/2} N_e N_i , \tag{1}$$

where g is a Gaunt factor[3] and where the other symbols have their usual meaning. For photon energies much higher than kT (as is the case in the absorbing shell), g is very nearly equal to 1, and Eq. (1) can be written

$$k_{ff}(\mathrm{cm}^{-1}) = 4.02 \times 10^{-51} Z^2 N_e N_i \lambda^3 / T^{1/2} , \tag{2}$$

where λ is in angstroms, N_e and N_i in cm^{-3}, and T is in keV. For a multispecies target, $Z^2 N_e N_i$ is replaced by $N_e^2 \langle Z^2 \rangle_{\mathrm{av}} / \langle Z \rangle_{\mathrm{av}}$ in terms of species averages. For a CH target, in terms of the mass density ρ ($g\ \mathrm{cm}^{-3}$), we find (assuming fully ionized CH)

$$k_{ff}(\mathrm{cm}^{-1}) = A_{\mathrm{CH}}\lambda^3\rho^2/T^{1/2}, \tag{3}$$

where $A_{\mathrm{CH}}=2.23\times10^{-3}$. From Eq. (3), an optical depth $\tau=k\Delta r$ of 1 will occur in CH at the photon energy E_1 given by

$$\rho^2\Delta r/T^{1/2} = 0.24\,E_1^3. \tag{4}$$

Because of the assumption of full ionization, Eq. (4) would be valid for temperatures higher than ~200 eV. As an example, assume an imploded CH shell target with $T=0.3$ keV, $\rho\Delta r=0.05$ g cm^{-2}, and $\rho=50$ g cm^{-3}; E_1 would then be at 2.66 keV.

The proposed diagnostic method relates the observed photon energy of the peak $E_{\max}$ to E_1, from which the quantity $\rho^2\Delta r/T^{1/2}$ for the shell is derived. Obviously, the optical depth at the peak would be of order 1: for photon energies lower than $E_{\max}$ the intensity falls because the optical depth is higher than 1, whereas above $E_{\max}$ the falling continuum is just the unattenuated core-emission spectrum. Because of the weak dependence on T, a crude knowledge of the temperature yields the quantity $\rho^2\Delta r$ through the cold part of the shell. This quantity, in conjunction with a separate determination of the $\rho\Delta r$ (for example, from nuclear activation) can be used to estimate the shell density. However, it should be noted that the nuclear activation technique measures $\rho\Delta r$ of the entire shell, not only its cold part.

In imploded glass shells with T ~300 eV (in the outer part of the imploded shell), silicon atoms will not be fully ionized (i.e., a significant fraction will have at least one bound electron), and photoionization will dominate the absorption. The photoionization opacity for energies above the Si K edge is then approximately given by the opacity of cold glass,[4] multiplied by a correction factor α. This factor accounts for the fact that the L shell will be totally ionized even at these temperatures, and is given in terms of the opacity based on the K and L shells, $\alpha = k_K/k_{K+L}$. From the measured opacity jump of cold material at the K edge we find $\alpha = 0.91$, and thus (from Ref. 4) $k_{bf}=8.76\,\lambda^3\rho$ (λ in angstroms). This equation applies to glass with mostly helium-like silicon ions. If most of the silicon ions are hydrogen-like, the opacity will be half of this. However, in typical cases the cold part of the imploded glass shell has only a small percentage of hydrogen-like silicon ions; the hotter layers contribute little to the overall opacity. An optical depth of 1 will be attained at an energy E_1 given by

$$E_1(\mathrm{keV}) = 25.5(\rho\Delta r)^{1/3}. \tag{5}$$

Because of the assumption of little ionization of K-shell silicon ions, Eq. (5) would be valid for temperatures lower than ~500 eV. For $\rho\Delta r = 0.05$ g cm^2 this relation gives $E_1 = 9.4$ keV, much higher than E_1 for the plastic-shell example given above; at this high photon energy the emitted intensity is small and difficult to detect above the background. This background is due mostly to radiation from the laser-target interaction region, and is higher for glass targets. Time-resolved spectroscopy can be used to greatly reduce the background problem.

In order to relate E_1 to E_{max}, the photon energy of the spectral peak, we approximate the emitted spectrum by the relation

$$I = I_0 \exp(-E / T_c) \exp\left[-(E_1 / E)^3\right]. \tag{6}$$

The first factor approximates the unattenuated x-ray flux as that emitted by a hot plasma at a single core temperature T_c (which is higher than the temperature T of the absorbing shell); the second factor accounts for the shell absorption and follows from Eq. (1) and the definition of E_1. It should be emphasized that for typical fuel-filled CH shells, most of the core radiation is emitted by the inner CH layer and thus T_c is lower than the peak fuel temperature. However, in very-high-density compressions the fuel emission can dominate the emission from the core, and T_c will then correspond to the fuel temperature. The emergent spectrum I of Eq. (6) has a peak E_{max} given by

$$(E_{max} / E_1) = (3T_c / E_1)^{1/4}. \tag{7}$$

To relate the measured E_{max} to E_1, T_c can be determined from the continuum slope at photon energies above the peak, and Eq. (7) can then be solved for E_1. The (E_{max}/E_1) ratio is typically close to 1 (see the following).

The assumption of negligible photoionization opacity in CH shells deserves some scrutiny. Since the cross section for photoionization is typically much larger than that for inverse bremsstrahlung, the former will be negligible only if the plastic shell is highly ionized everywhere. An ionization rate-equation code (POPION[5]) has shown that the ionization of carbon at the expected temperatures of the compressed plastic shell is incomplete. For example, at a temperature of 200 eV and an electron density of 1×10^{24} cm^{-3}, the fraction of carbon ions in the hydrogen-like state is 32%, and at 300 eV it is 14% (most of the rest is stripped). We estimate now the ratio of the two opacity contributions, k_{bf} caused by photoionization and k_{ff} arising from inverse bremsstrahlung. k_{ff} is given by Eq. (3) where ρ is now written as ρ_s, the density of completely ionized (stripped) material. k_{bf} is taken as the measured opacity[4] of cold CH, in terms of the density ρ_{us} of the unstripped carbon, multiplied by the correction factor $\alpha = 0.96$, then divided by 2 (because most of the unstripped carbon will be in the hydrogen-like state, whereas the cold-material formula assumes two K-shell electrons):

$$k_{bf} = 0.54 \lambda^3 \rho_{us}, \tag{8}$$

so that the ratio of the two becomes

$$R_k = k_{bf} / k_{ff} = 242 (T^{1/2} / \rho_{us}) (\rho_{us} / \rho_s). \tag{9}$$

As an example, assuming $T = 0.2$ keV and a fraction of unstripped material of 0.2, R_k will be smaller than 1 only at densities higher than 22 g cm^{-3}. Thus, a more detailed calculation with a numerical code is required to determine the relative importance of these two absorption mechanisms for target experiments of lower densities.

Comparison with Code Calculations

We next compare the location of the peak as predicted by Eqs. (4) or (5) with that predicted by a hydrodynamic code (*LILAC*), run in conjunction with a non-LTE post processor that calculates the emergent radiation spectrum.[6] We first simulate the implosion of a DD-filled CH shell. Fig. 47.14 shows the calculated, time-integrated emergent spectrum from a CH shell of 10-μm thickness and 250-μm diameter, filled with 40-atm pressure of D_2, irradiated by a 1.25-kJ, 625-ps (FWHM) laser pulse ($\lambda = 351$ nm). It should be noted that the computed spectrum results from radiation-transport treatment that sums over rays of different impact parameters (the ray geometry can be described as a set of concentric cylinders intersecting the spherical target). Thus, it corresponds to a spectral measurement without any spatial resolution. Obviously, even with no such resolution, a peak in the spectrum should be evident. Spatial resolution would increase the contrast of the peak in the spectrum; the most distinct peak being in the spectrum viewed through the target center. The two additional curves in Fig. 47.14 correspond to simulations where the contribution of only free-free or only bound-free transitions to the opacity were included. It is clear that the contribution of free-free transitions accounts for much of the opacity. By removing either contribution to the opacity, the emergent radiation suffers less attenuation in the shell and is therefore stronger; also, the peak shifts to lower photon energies, where the absorption is higher. The peak E_1 given by Eq. (4) can now be compared with the peak of the curve marked FF in Fig. 47.14. The integral $\int \rho^2 dr$ over the entire CH shell of Fig. 47.14, at peak compression, was calculated by the code to be 1.27 $g^2\,cm^{-5}$. Substituting into Eq. (4), and using the average simulated shell temperature at peak compression of 0.35 keV, we obtain $E_1 = 2.08$ keV. The continuum slope in Fig. 47.14 gives $T_c = 1.2$ keV, and Eq. (7) then yields $E_{max} = 2.38$. This position of the peak agrees to within

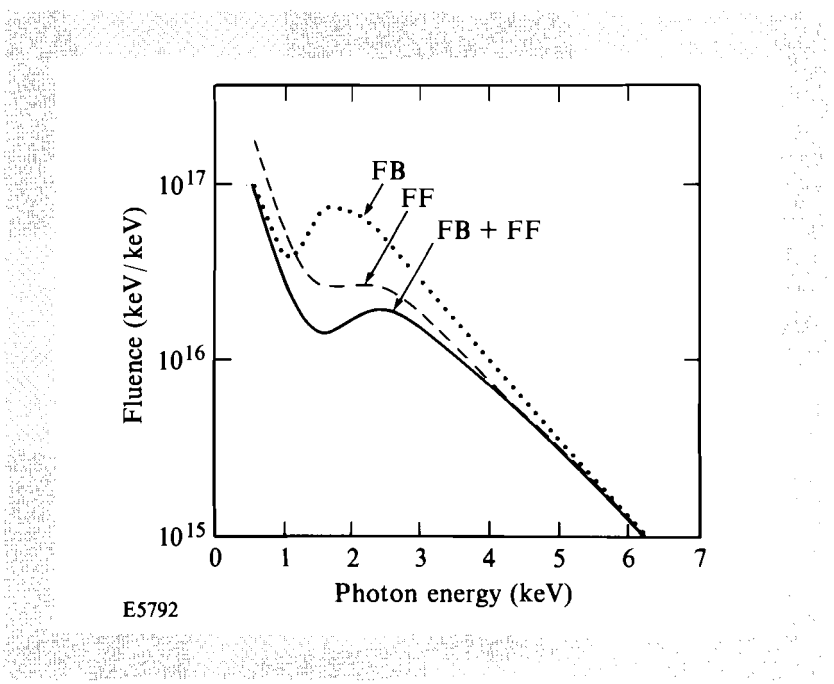

Fig. 47.14
Calculated emergent spectrum (time integrated) from a CH shell of 10-μm thickness and 250-μm diameter, filled with 40-atm pressure of D_2, irradiated by a 1.25-kJ, 625-ps (FWHM) laser ($\lambda = 351$ nm). For the curve marked FB, only the bound-free contribution to the opacity was included in the simulation; for the curve marked FF, only the free-free contribution to the opacity was included. The curve marked FB + FF corresponds to the full calculation.

better than 10% with the peak in the simulated spectrum marked FF in Fig. 47.14. This agreement indicates that the time-integrated spectrum can be used to derive the $\rho^2\Delta r$ value at the time of peak compression. In fact, a closer examination of the computation shows that the peak is typically formed over a ~50-ps period around peak compression; time integration reduces the ratio of peak height to background but has little effect on the position of the peak. This agreement also shows that the derived $\rho^2\Delta r$ value (which is only related to the absorbing part of the shell) is only slightly less than that for the total shell thickness. Indeed, the computations show that around peak compression, the inner third of the shell is hot (~1 keV) and is the source of the emitted continuum. As previously discussed, even the hot CH layer contributes to the continuum absorption; therefore the derived value of $\rho^2\Delta r$ (related only to the absorbing layer) is quite close to the $\rho^2\Delta r$ value of the entire shell thickness.

We next verify that, as expected, the peak in the emergent spectrum shifts to higher photon energies for higher compression implosions. To that end, we compare in Fig. 47.15 the spectrum from Fig. 47.14 with that of a thicker CH shell, imploded by a higher-energy laser: the shell thickness is now 15 μm (as compared with 10 μm), and the laser energy is now 1.87 kJ, as compared with 1.25 kJ. All other parameters are the same for the two simulations. The results of Fig. 47.15 are not time integrated but, to enhance the contrast they show the spectral energy per nanosecond at the time of peak compression. The integral $\int\rho^2 dr$ over the the thicker CH shell, at peak compression, was calculated by the simulation to be 5.95 $g^2\ cm^{-5}$ (as compared with 1.27 $g^2\ cm^{-5}$ for the thinner shell). The temperature is also higher, 0.64 keV as compared with 0.34 keV. Using Eqs. (4) and (7) as before, we find E_{max} = 3.25 keV, in good agreement with the thicker-shell curve of Fig. 47.15. Comparison of the Figs. 47.14 and 47.15 shows that, even though

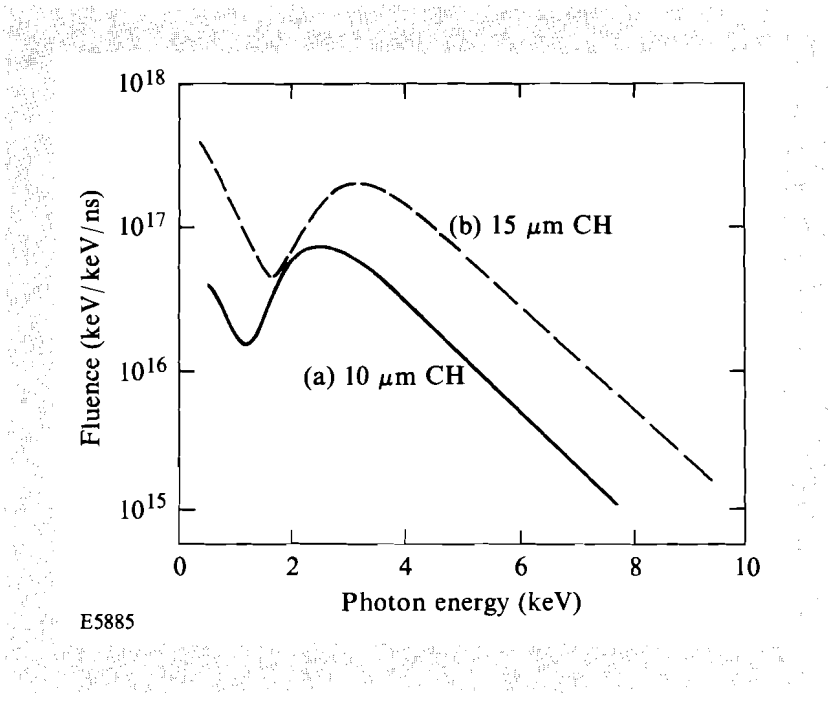

Fig. 47.15
Comparison of the calculated emergent spectrum (per nanosecond at the time of peak compression) from (a) the shell of Fig. 47.14, and (b) a 15-μm-thick shell irradiated with a 1.87-kJ laser pulse. All other parameters are the same for the two shots.

the peak is still visible in the time-integrated results, a better contrast would be obtained with a time-resolved measurement; however, the position of the peak itself is hardly affected.

The comparison with the code simulations shows, thus, that the simple relationship for CH shells given by Eq. (4) provides a fairly good estimate of the shell $\rho^2\Delta r$. In actual application of the method, the measured position of the peak will be compared with the results of full simulations. In the case of agreement in the position of the peak, we can surmise that the predicted $\rho^2\Delta r$ has been achieved. However, in the case where the two disagree (because of a degradation in implosion performance), Eq. (4) could be used to estimate the reduction in $\rho^2\Delta r$, corresponding to a measured shift in E_{max} with respect to the predicted value.

Discussion

The applicability of the method for cases of instability and shell-fuel mixing requires special attention. If the instability does not lead to shell breakup or severe shell distortion, and a peak in the emitted spectrum is still observed, it is very likely that Eq. (4) will still be applicable. The instability in this case will be manifested by a reduced shell $\rho^2\Delta r$ (or $\rho\Delta r$) and a reduced core temperature (due to either radiation cooling or incomplete conversion of kinetic to thermal energy). The position of the peak will then show the reduced $\rho^2\Delta r$ (by appearing at a lower photon energy) and the continuum slope beyond the peak will show the reduced core temperature. The application of Eq. (4) is valid provided that the carbon in the target is almost completely stripped. This requires the temperature in the cold part of the CH shell to exceed ~200 eV. The application of Eq. (5) to determine the $\rho\Delta r$ of the cold part of the shell only requires that silicon ions there have at least two bound electrons, or that the temperature be lower than ~500 eV. Thus, the achievement of lower than predicted temperature because of instability will only improve the applicability of Eq. (5) and will invalidate Eq. (4) only if the cooling was very severe.

Severe shell deformation could be demonstrated by observing a different position of the peak in the spectrum, when viewed from two different directions. Shell breakup will result in smearing and eventually the disappearance of the spectral peak. This is because different parts of the core radiation now traverse different $\rho\Delta r$ segments, leading to peaks of different spectral position. Thus, an indistinct peak in the observed spectrum could be indicative of an unstable implosion.

ACKNOWLEDGMENT

This work was supported by the U.S. Department of Energy Office of Inertial Confinement Fusion under agreement No. DE-FC03-85DP40200 and by the Laser Fusion Feasibility Project at the Laboratory for Laser Energetics, which is sponsored by the New York State Energy Research and Development Authority and the University of Rochester.

REFERENCES

1. LLE Review **24**, 169 (1985).

2. L. Spitzer, *Physics of Fully Ionized Gases*, 2nd Rev. Ed. (Interscience, New York, 1962), p. 148.
3. W. J. Karzas and R. Latter, *Astrophys. J. Supp.* **6**, 167 (1961).
4. B. L. Henke and R. L. Elgin, *Advances in X-Ray Analysis* **13**, 1 (1969).
5. R. Epstein, S. Skupsky, and J. Delettrez, *J. Quant. Spectrosc. Radiat. Transfer* **35**, 131 (1986).
6. R. Epstein, *Phys. Fluids B* **1**, 214 (1989).

1.C Fokker-Planck Simulations of Laser Filamentation in Plasmas

In inertial confinement fusion (ICF), where irradiation uniformity is a crucial issue, it is important to understand the process of laser-filamentation instability.[1] The breakup of laser light into filaments occurs as a result of plasma density depressions that form localized focusing channels. The density depressions may be caused either by ponderomotive forces[2] due to laser-plasma interactions or by thermal forces[3] arising from collisional light absorption. The main consequences of the instability are that high-intensity laser irradiation in the filaments can generate ablation-pressure nonuniformities in ICF targets and give rise to undesirable parametric instabilities.[1]

There have been extensive theoretical and experimental efforts to understand and characterize filamentation.[1-6] Recently, Young *et al.*[4] have attempted to generate and identify filaments under controlled experimental conditions, in which a fairly homogeneous plasma was irradiated by a spatially modulated laser beam. By comparing their observations with analytic predictions based on ponderomotive and thermal-filamentation growth rates, they concluded that the ponderomotive mechanism was responsible for the occurrence of filaments. However, a subsequent improved theory of filamentation that took into account nonlocal heat transport effects indicated that the thermal rather than the ponderomotive mechanism may have been responsible for their experimental observations.[5] The main purpose of this article is to confirm this hypothesis by simulating as closely as possible the reported experimental conditions using the two-dimensional (2-D) Fokker-Planck (FP) code SPARK.[7] Also, by doing parallel simulations invoking classical transport [with Spitzer-Härm[8] (SH) heat flow], general contributions from kinetic effects are demonstrated.

In contrast to the analytic theories that assume linear departure from energy and momentum balance to calculate exponential growth rates, the code models the full hydrodynamic response of the ions (assumed cold), the electron heat flow using the FP equation, and the paraxial wave equation for the laser light. The following sections describe the modeling in more detail, Young *et al.*'s experimental conditions and results, the simulation results, and finally the discussion and conclusions.

Description of the Model

In this article the plasma is assumed to be in planar x-z geometry, where **z** is the direction of laser propagation. The present version of the 2-D Eulerian code SPARK is comprised of three main parts: (A) a laser-propagation routine based on the paraxial wave equation; (B) an electron-transport routine that solves the FP equation in the center-of-mass frame of the ions; and (C) an ion-transport routine that advances ion density and momentum under the influence of the electron and ponderomotive pressures. These are described briefly as follows.

(A) Laser Propagation

Using the paraxial approximation, the time-averaged electric field $\mathbf{E}_L(x,z)$ of a laser is defined by[3]

$$\mathbf{E}_L(x,z) = \left[\frac{8\pi}{c^2 k(z)}\right]^{1/2} \mathbf{F}(x,z)\exp\left[i\int_0^z k(z')dz'\right], \tag{1}$$

where $k(z) = (\omega/c)\,[1-\omega_p{}^2(0,z)/\omega^2]^{1/2}$, ω_p is the plasma frequency, and ω is the angular frequency of the laser. Substituting Eq. (1) for the electric field into Maxwell's equations, we obtain the following result [3]

$$\frac{\partial \mathbf{F}}{\partial z} = \frac{i}{2k}\left\{\frac{\partial^2 \mathbf{F}}{\partial x^2} - \frac{\omega_p^2(x,z)}{c^2}\left[1-\omega_p^2(0,z)/\omega_p^2(x,z)\right]\mathbf{F} + ik(z)K_{ib}(x,z)\mathbf{F}\right\}, \tag{2}$$

where K_{ib} is the attenuation coefficient for collisional absorption. This so-called paraxial wave equation assumes that the light wave propagates infinitely fast across the plasma and that $|k(z)^{-1}(\partial \mathbf{F}/\partial z)| << |\mathbf{F}|$. Its numerical solution is accomplished via standard finite difference techniques (see Ref. 6).

(B) Electron Transport

The electron-transport model is based on the diffusive approximation to the FP equation, without magnetic fields. Such a model has been successfully used to model 2-D electron transport in laser-produced plasmas.[7] Although the equations and methods of solution have been described in detail in Ref. 7, a few modifications have been introduced here. By defining the electron-distribution function in the frame of the moving ions (with velocity $\mathbf{u}_i$), the equations describing the evolution of the isotropic and anisotropic part of the distribution become

$$\frac{\partial f_o}{\partial t} + \mathbf{u}_i \bullet \nabla f_o - \nabla \bullet \mathbf{u}_i \frac{v}{3}\frac{\partial f_o}{\partial v}$$

$$= -\frac{v}{3}\nabla \bullet \mathbf{f}_1 + \frac{1}{v^2}\frac{\partial}{\partial v}\left\{\frac{v^2}{3}\mathbf{a} \bullet \mathbf{f}_1 + Y\left[Cf_o + \left(D + \frac{nZ^* v_o^2}{6v}\right)\frac{\partial f_o}{\partial v}\right]\right\}, \tag{3a}$$

$$\mathbf{f}_1 = -\tau\left(v\nabla f_o - \mathrm{a}\partial f_o / \partial v\right), \tag{3b}$$

where $\mathbf{a} = |e|\mathbf{E}/m$, $Y = 4\pi(e^2/\mathrm{m})^2 \ln\Lambda$, e is the electric charge, m is the electron mass, $\ln\Lambda$ is the Coulomb logarithm, C and D are the Rosenbluth potentials (defined in Ref. 9), v_o is the electron oscillatory velocity in the laser field, and $Z^* = \langle Z^2 \rangle / \langle Z \rangle$ is the effective ionization number (where $\langle\,\rangle$ denotes an average over the ion species). Here the 90° angular scattering collision time is given by $\tau = v^3/[\phi Z^* nY]$, where $n = \langle Z \rangle n_i$ is the electron number density (assuming quasi-neutrality) and $\phi = (Z^* + 4.2)/(Z^* + 0.24)$. The inclusion of a factor ϕ in the definition of τ is an attempt at correcting for the high-Z (or Lorentz) approximation in Eq. (3b). Such a correction is found to give the *exact* heat flow coefficient when f_0 is Maxwellian.

The second and third terms on the left-hand side of Eq. (3a) represent the hydrodynamic contribution to the transport. For computational purposes it has been found convenient to rewrite them in the form

$$\nabla \bullet (\mathbf{u}_i f_0) - \nabla \bullet \mathbf{u}_i \left(1 + \frac{v}{3} \frac{\partial}{\partial v} \ln f_0 \right) f_0 ,$$

such that the first term is now expressed in conservative form. The reason for using a logarithmic derivative in the second term is that it can be approximated as $\partial_v \ln f_{0,j} = [\ln(f_{0,j+1}/f_{0,j-1})]/2\Delta v_j$, where Δv_j is the magnitude of the velocity mesh at the jth cell. This formulation ensures zero truncation error for a Maxwellian f_0 and minimizes departures from quasi-neutrality.

The solution for f_0 is accomplished by substituting Eq. (3b) into (3a) and differencing the result in an orthogonal mesh (x_l, z_k, v_j), where the subscripts denote cell centers. The left-hand side of Eq. (3a) is advanced explicitly in time using a standard donor-cell scheme.[10] The remaining part of the equation is solved by an "alternating-direction-implicit" method, in the manner described in Ref. 7. Quasi-neutrality is enforced by requiring zero current $\mathbf{j} = -(4\pi e/3) \int dv\, v^3 \mathbf{f}_1$ and calculating the electric field accordingly.

(C) Ion Transport

Conservation of density and momentum for cold ions is given by

$$\frac{\partial n_i}{\partial t} + \nabla \bullet (n_i \mathbf{u}_i) = 0 , \tag{4}$$

$$\frac{\partial (n_i m_i \mathbf{u}_i)}{\partial t} + \nabla \bullet (n_i m_i \mathbf{u}_i \mathbf{u}_i) = -\nabla p + \mathbf{P}_F , \tag{5}$$

where m_i is the ion mass, $p = (4\pi/3) \int dv\, v^4 f_0$ is the electron pressure,

$$\mathbf{P}_F = -\frac{\omega_p^2(x,z)}{2\omega^2} \nabla \left[\frac{|\mathbf{F}|^2}{v_g(z)} \right]$$

is the ponderomotive force, and where $v_g = k(z)c^2/\omega$ is the group velocity of the light wave. Equations (4) and (5) are solved using donor-cell differencing (without artificial viscosity).

At each time step, SPARK solves not only Eqs. (1) to (5) but also an equivalent set of equations where Eq. (3) becomes the energy conservation relation under the assumption of classical heat transport,[8] i.e., $q_{SH} = -\kappa_{SH}\nabla T$, with κ_{SH} being the SH heat-flow coefficient. In order to ensure a meaningful comparison between classical and kinetic transport results, the code is regularly tested in the collisional limit where both are expected to converge.

Young *et al.*'s Experimental Conditions and Results

In Young *et al.*'s[4] experiment a CH-foil target was irradiated by laser light to form a fairly homogeneous underdense plasma. The plasma was subsequently irradiated by a 1.06-μm interaction beam with a 100-ps FWHM pulse. This beam was spatially modulated in the transverse x direction, such that $\delta I/I_0 = 0.81$, where I_0 is the peak laser intensity and $\delta I = (I_0 - I_{min})$. A separate 0.35-μm beam with the same pulse length was synchronized with the interaction beam to probe for the formation of filaments. The refraction of the probe light through the plasma gave a measure of its density modulation $\delta n/n_0$, which in turn provided an indirect measure of the level of filamentation.

It was reported that, for a transverse spatial modulation $\lambda_\perp = 42$ μm and $I_0 = 4.2 \times 10^{13}$ W/cm^2, laser filamentation was observed with an estimated $\delta n/n_0 \sim 10\%$. No filamentation was observed for a 135-μm wavelength with $I_0 = 4.2 \times 10^{13}$ W/cm^2, nor for a 42-μm wavelength with $I_0 = 2.8 \times 10^{13}$ W/cm^2.

The plasma background conditions at the time of the interaction beam have been simulated by LASNEX, the results of which were presented in Young *et al.*'s paper.[4] For our purpose the plasma is assumed to have a spatial extent of 400 μm, with a parabolic density profile in the z direction approximated by

$$\frac{n}{n_c} = 0.25\left[1 - 0.124\left(\frac{z-400}{182}\right)^2\right],$$

such that the density ranges from 0.1 n_c to 0.25 n_c, where n_c is the critical density. Since $\lambda_\perp$ is much smaller than the density scale length in the transverse direction, the plasma is assumed to be uniform in that direction. A temperature of 0.8 keV was taken throughout the plasma.

The interaction beam is modeled by $I(t) = I_0(t)(1 + \varepsilon \cos k_\perp x)$, where $k_\perp = 2\pi/\lambda_\perp$ and $\varepsilon = 0.68$. Its temporal evolution is Gaussian with a 100-ps FWHM.

Simulation Results

Simulation results are presented here with the initial background conditions described in the previous section and three types of interaction beams, with varying spatial modulation wavelengths and peak intensities. In all cases the plasma is defined in a uniform 20 × 20 Eulerian grid in the x-z plane, with 18 velocity groups of size $\Delta v = 0.5(T/m)^{1/2}$ (where $T = 0.8$ keV). In view

of the symmetry of the problem, the simulation is restricted to $0 \le x \le \lambda_\perp/2$, with reflective boundary conditions imposed at $x = 0$ and $\lambda_\perp/2$. Zero heat flow is likewise imposed at the $z = 0$ and 400-μm boundaries, though free plasma flow is allowed there.

All simulations progress from −100 ps to 100 ps with respect to the peak of the interaction pulse. The time step and grid size were small enough to ensure converging solutions and a maximum fractional deviation from quasi-neutrality of less than 1%.

(A) $I_0 = 4.2 \times 10^{13}$ W/cm^2 and $\lambda_\perp = 42$ μm

Figure 47.16 shows a surface plot of the normalized laser intensity I/I_0 in the x-z plane at $t = -100$ ps. The plot emphasizes the initial spatial modulation of the interaction beam and shows that the beam is slightly attenuated as it propagates through the plasma.

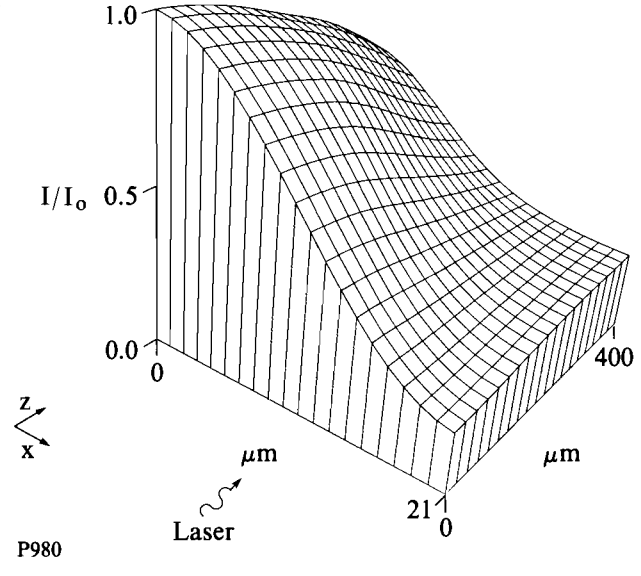

Fig. 47.16
Surface plot of normalized initial laser intensity I/I_0 on the x-z plane.

At the peak of the pulse there is significant amplification of the laser intensity due to self-focusing, as shown in Fig. 47.17(a). By comparison, the case with SH heat flow, depicted in Fig. 47.17(b), shows very little self-focusing. This gives a clear indication that nonlocal (or kinetic) heat transport plays a significant role in the filamentation process. Indeed, if one were to repeat the same simulation with the ponderomotive force artificially suppressed, the peak intensity in Fig. 47.17(a) would only go down by 30%, whereas in the classical transport case the amplification would disappear completely. The dominance of kinetic thermal filamentation can be directly attributed to the reduction in the effective heat-flow coefficient, as discussed in Ref. 5. For the present case, the ratio of the FP heat flow $\mathbf{q}_{FP}$ to the local $\mathbf{q}_{SH}$ ranges from 0.1 to 0.003 across the mesh, despite the fact that the

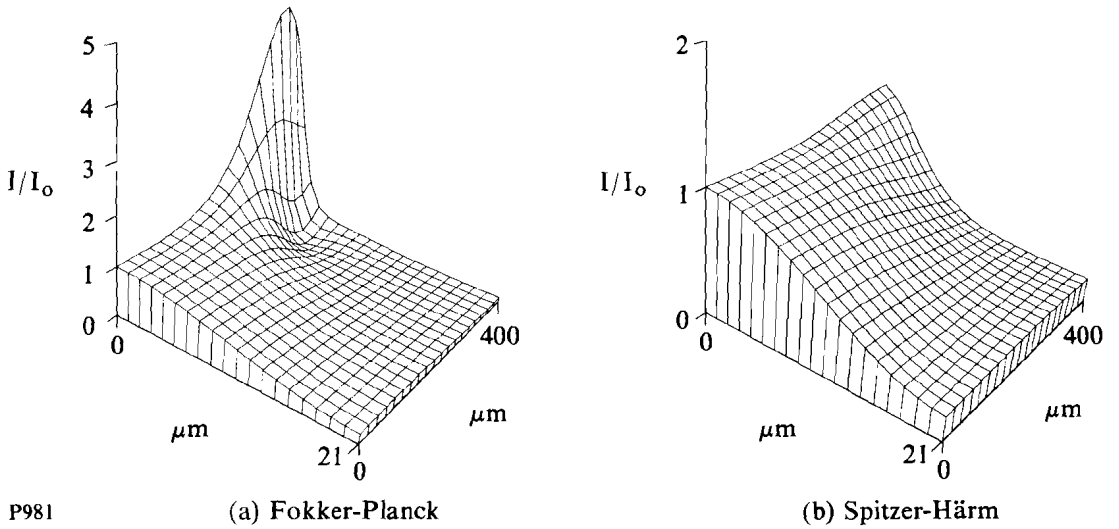

Fig. 47.17
Surface plots of I/I_0 on the x-z plane at $t = 0$ ps (i.e., at the peak of the laser pulse) for (a) Fokker-Planck transport and (b) Spitzer-Härm transport.

magnitude of $\mathbf{q}_{FP}$ never rises above 0.006 q_f, where $q_f = nm(T/m)^{3/2}$ is the so-called free-streaming limit.

The main diagnostic for filamentation in Young *et al.*'s experiment[4] measures density modulation, rather than intensity amplification. Therefore, $\delta n/n_0 = (n - n_0)/n_0$ [where $n_0(z)$ is the mean density averaged along x] is plotted in Figs. 47.18(a) and 47.18(b) for nonlocal and classical transport, respectively. Although $\delta n/n_0$ in Fig. 47.18(a) is somewhat smaller than the 10% measured experimentally, this discrepancy could be attributed to the uncertainties in the experimental measurement and in the quoted plasma background conditions. However, it is certainly clear that the ponderomotive force alone, which is the dominant driving mechanism in Fig. 47.18(b), yields $\delta n/n_0$ values that are more than one order of magnitude below 10%.

Another important factor in the interpretation of these simulations is the temporal evolution of the plasma. This is described in Fig. 47.19, which plots the σ_{rms} of n (i.e., the maximum rms deviation of n across x, normalized to n_0), for FP transport (solid curve) and SH transport (dashed curve) as a function of time. It is obvious from the transient nature of the curves that steady state (or pressure balance) is never achieved in the simulation. This fact could have been predicted by estimating the hydrodynamic response time of the plasma as $\tau_H = \lambda_\perp/c_s$, where c_s is the isothermal sound speed. For our conditions $\tau_H \sim 200$ ps, which is comparable to the FWHM of the laser. From the point of view of Young *et al.*'s experiment,[4] the probe beam was able to detect the density modulations since it was synchronized with the interaction beam (with the same 100-ps FWHM).

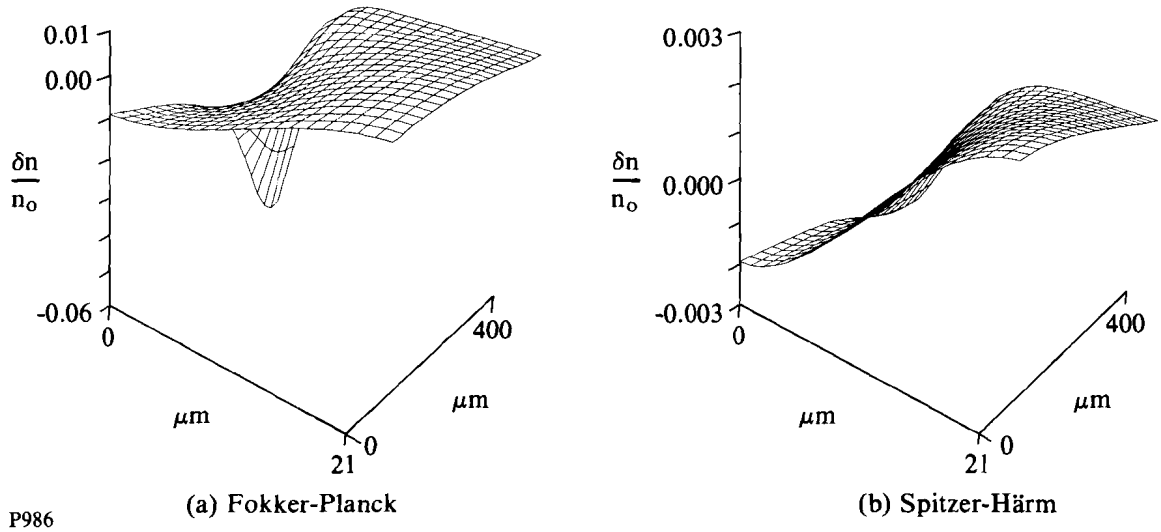

Fig. 47.18
Surface plots of normalized density modulation $\delta n/n_0$ on the x-z plane at $t = 0$ ps for (a) Fokker-Planck transport and (b) Spitzer-Härm transport. Note that $\delta n/n_0$ changes sign from < 0 at $x = 0$ (representing a depression) to > 0 at $x = 21$ μm.

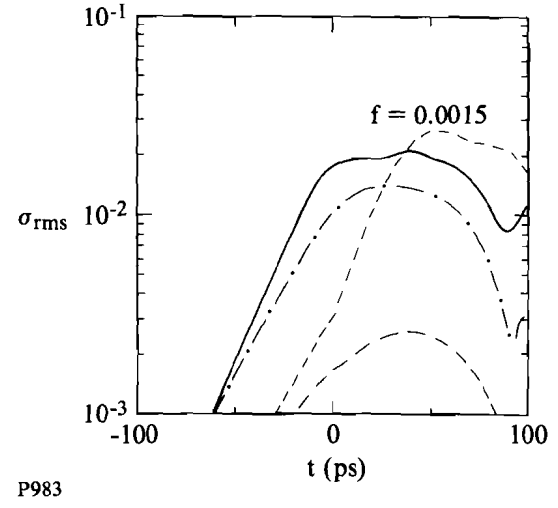

Fig. 47.19
Plot of rms density modulation σ_{rms} as a function of time, for case (A) $I_0 = 4.2 \times 10^{13}$ W/cm^2 and $\lambda_\perp = 42$ μm. Solid curve corresponds to Fokker-Planck simulation, dash-dotted curve to Fokker-Planck simulation without ponderomotive force, and dashed curves to Spitzer-Härm simulation (with and without a flux limiter).

To re-emphasize the dominance of the kinetic thermal-filamentation instability over the ponderomotive one, Fig. 47.19 also plots the FP simulation results without the ponderomotive force (dash-dotted curve). The corresponding curve with SH heat flow is not displayed since its $\sigma_{rms} << 10^{-3}$.

In an attempt to reproduce the FP results, the SH simulation was repeated by limiting the heat flux with a harmonic flux limiter, i.e., $\mathbf{q}_{SH}/(1 + |\mathbf{q}_{SH}/fq_f|)$.[11] It was found that $f = 0.0015$ gave the best fit, though the agreement was qualitative at best (see dashed curve identified by $f = 0.0015$ in Fig. 47.19). Another problem with the flux limiter is that the appropriate f would have to depend on $\lambda_\perp/\lambda_e$ because the amount of heat-flux inhibition due to nonlocal transport effects is dependent on $\lambda_\perp/\lambda_e$, where $\lambda_e = T^2/[4\pi ne^4(\phi Z^*)^{1/2}\ln\Lambda]$ is the effective stopping length of an electron.[12]

(B) $I_0 = 2.8 \times 10^{13}$ W/cm^2 and $\lambda_\perp = 42$ μm

These parameters for the interaction beam give rise to qualitatively similar results to case (A). As expected, the reduction in peak laser intensity has the effect of reducing the degree of self-focusing and the amount of density modulation. The temporal response of the latter is plotted in Fig. 47.20, which shows approximately a 25% reduction in the maximum σ_{rms} from that in Fig. 47.19. It is, therefore, surprising that in this case no filamentation was observed experimentally. One could speculate that this present case happens to fall just below the detection threshold of the experiment.

(C) $I_0 = 4.2 \times 10^{13}$ W/cm^2 and $\lambda_\perp = 135$ μm

In this case, no filaments were detected experimentally.[4] The results of the simulation, plotted as density σ_{rms} as a function of time in Fig. 47.21, confirm these findings. Since the hydro response time ($\tau_H \sim 600$ ps) is longer for this case than for cases (A) and (B), the density-modulation level is too low at the peak of the probe beam to be measured. The σ_{rms} eventually reaches $\sim 10^{-2}$ at $t = 100$ ps; however, by then the probe beam is too weak to detect it. Therefore, the reduction in the level of self-focusing has less to do with the spatial growth rate of the instability and more to do with the hydrodynamic response of the plasma.

Discussion and Conclusions

The results presented in this article are in qualitative agreement with the analytic kinetic theory of filamentation derived in Ref. 5, which predicted larger growth rates for the thermal rather than ponderomotive filamentation. However, quantitative comparisons have not been possible since that theory calculates linear spatial growth rates for a given transverse spatial modulation $k_\perp$, assuming momentum and energy balance. Despite the fact that $|\delta n/n_0|$ and $|\delta T/T_0| << 1$, the FP simulations yield $\delta I/I_0 >> 1$ and a corresponding wide spectrum in $k_\perp$, in accordance with the narrowing of the filaments as they propagate along **z**. Moreover, steady-state conditions are never achieved. In fact, by observing the time behavior of the density in Fig. 47.19 one can see the onset of spatial oscillations (of period τ_H) for $t \gtrsim 100$ ps. The total amount of damping may, however, be underestimated since SPARK does not include Landau damping.[13]

Although we have only considered 2-D filamentation, in some circumstances three-dimensional effects could become important and give rise to considerably larger intensity amplifications.[14] This is specially true if "hot-

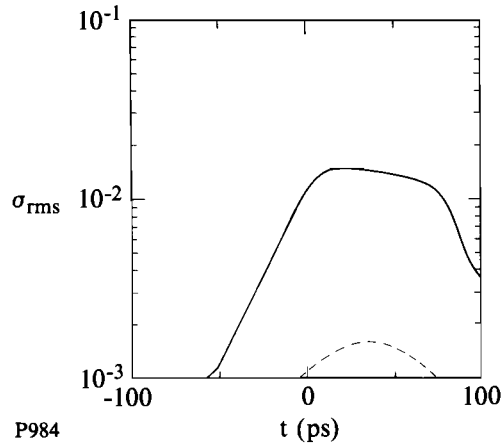

Fig. 47.20
Plot of rms density modulation σ_{rms} as a function of time, for case (B) $I_0 = 2.8 \times 10^{13}$ W/cm^2 and $\lambda_\perp$ = 42 μm. Solid curve corresponds to Fokker-Planck simulation, and dashed curve to Spitzer-Härm simulation.

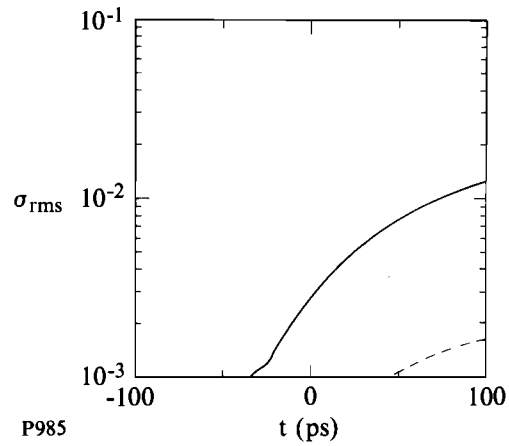

Fig. 47.21
Plot of rms density modulation σ_{rms} as a function of time, for case (C) $I_0 = 4.2 \times 10^{13}$ W/cm^2 and $\lambda_\perp$ = 135 μm. Solid curve corresponds to Fokker-Planck simulation, and dashed curve to Spitzer-Härm simulation.

spots" are present in the laser-intensity profile, since these may give rise to cylindrical instead of planar filaments. However, the conclusions regarding the comparison between thermal and ponderomotive filamentation are likely to remain unchanged.

The role of magnetic fields in the presence of nonuniform laser illumination has been previously studied in the context of 2-D classical heat flow and found to be negligible.[15] The effects of magnetic fields on nonlocal transport are expected to be stronger,[16] though an accurate estimation of their importance is outside the scope of this work.

In conclusion, the dominance of kinetic thermal filamentation over ponderomotive filamentation, predicted by analytic theory, has been confirmed by means of the 2-D FP code SPARK. Specific simulations using the reported conditions of Young *et al.*'s experiment show good agreement with their results.

ACKNOWLEDGMENT

We wish to thank Drs. R. L. Berger, B. F. Lasinski, and E. A. Williams for many useful discussions. This work was supported by the U.S. Department of Energy Office of Inertial Confinement Fusion under agreement No. DE-FC03-85DP40200 and by the Laser Fusion Feasibility Project at the Laboratory for Laser Energetics, which is sponsored by the New York State Energy Research and Development Authority and the University of Rochester.

REFERENCES

1. W. L. Kruer, *Comments Plasma Phys. Control. Fusion* **9**, 63 (1985); P. E. Young, *Comments Plasma Phys. Control. Fusion* **12**, 53 (1988); and references therein.
2. P. Kaw, G. Schmidt, and T. Wilcox, *Phys. Fluids* **16**, 1522 (1973).
3. M. S. Sodha, A. K. Ghatak, and V. K. Tripathi, in *Progress in Optics*, edited by E. Wolf (North Holland, Amsterdam, 1976), Vol. 13, p. 169; J. N. McMullin, C. E. Capjack, and C. R. James, *Comput. Phys. Commun.* **23**, 31 (1981).
4. P. E. Young *et al.*, *Phys. Rev. Lett.* **61**, 2336 (1988).
5. E. M. Epperlein, *Phys. Rev. Lett.* **65**, 2145 (1990).
6. B. I. Cohen *et al.*, *Phys. Fluids B* **3**, 766 (1991).
7. E. M. Epperlein, G. J. Rickard, and A. R. Bell, *Phys. Rev. Lett.* **61**, 2453 (1988); E. M. Epperlein, G. J. Rickard, and A. R. Bell, *Comput. Phys. Commun.* **52**, 7 (1988); G. J. Rickard, A. R. Bell, and E. M. Epperlein, *Phys. Rev. Lett.* **62**, 2687 (1989).
8. L. Spitzer, Jr. and R. Härm, *Phys. Rev.* **89**, 977 (1953).
9. I. P. Shkarofsky, T. W. Johnston, and M. A. Bachynsky, *The Particle Kinetics of Plasmas* (Addison-Wesley, London, 1966).
10. R. A. Gentry, R. E. Martin, and B. J. Daly, *J. Comp. Phys.* **1**, 87 (1966).
11. R. C. Malone, R. L. McCrory, and R. L. Morse, *Phys. Rev. Lett.* **34**, 721 (1975).
12. This definition of λ_e is slightly different from the one found in Ref. 5, due to the finite Z corrections currently introduced.
13. R. L. Berger, B. F. Lasinski, and E. A. Williams (private communication).
14. A. J. Schmitt, *Phys. Fluids B* **3**, 186 (1990); R. L. Berger *et al.*, in *Three-Dimensional Simulations of Filamentation* (presented at the 21st Anomalous Absorption Conference, Banff, Alberta, Canada, 15–19 April 1991).
15. A. R. Bell and E. M. Epperlein, *Plasma Phys. Control. Fusion* **28**, 897 (1986).
16. T. H. Kho and M. G. Haines, *Phys. Fluids* **29**, 2665 (1986).

Section 2
ADVANCED TECHNOLOGY DEVELOPMENTS

2.A Picosecond Characterization of Bent Coplanar Waveguides

Many of today's experimental electronic devices can successfully operate at frequencies far above 100 GHz. However, at these frequencies, characteristics of the interconnecting medium often become the limiting factor in the overall performance of high-speed circuits, restricting their maximum operating bandwidth. Speed limitations imposed by the interconnects will be even more severe in future high-speed, very-large-scale integrated (VLSI) circuitry, where the system complexity will force the designers to widely implement bent interconnects.

The studies of straight, coplanar transmission-line structures, suitable for high-speed interconnects, have been the subject of intensive research in the past.[1–7] Both room temperature[1–4] and superconducting (low-T_c[5] and high-T_c[6,7]) lines have been investigated. On the other hand, the previous studies of bent coplanar transmission lines were primarily limited to the low-frequency regime, where the bends were treated as point discontinuities.[8]

In this article we present the first sub-THz, time-domain characterization of bent transmission lines. For our studies we selected the coplanar waveguide (CPW) because it is a planar structure with comparatively low dispersion, low inductance, and low substrate sensitivity. Thus, it can be successfully implemented in a high-frequency regime.[9] We show that at sub-THz frequencies, bends in the CPW cannot be treated as point discontinuities and signal propagation along the bend must be included in the analysis. Never-

theless, we demonstrate that bent CPW's, especially those with curved or chamfered bends, can sustain low-distortion propagation up to about 100 GHz.

Experiment

The CPW's studied in this work are schematically shown in Fig. 47.22. In each case the transmission line formed a meander-like structure in order to measure cumulative distortion of the signal as it propagated along many bends. The CPW's were made of Au on undoped (semi-insulated) 500-μm-thick GaAs substrates, using a standard lift-off technique. The metal lines were 50 μm wide and 250 nm thick. The line separation was also 50 μm. Seven bent CPW's with different degrees of bend smoothing were fabricated in the same run. Each CPW was about 10 mm long and incorporated 20 bends over this distance, as well as the photoconductive switch (see Fig. 47.22). For comparison, a straight CPW of the same dimensions was also fabricated and tested. Figure 47.22 presents only the extreme cases and shows the right-angle-bent line (No. 1) and the lines with the bends smoothed by chamfering (No. 3) or curving (No. 6).

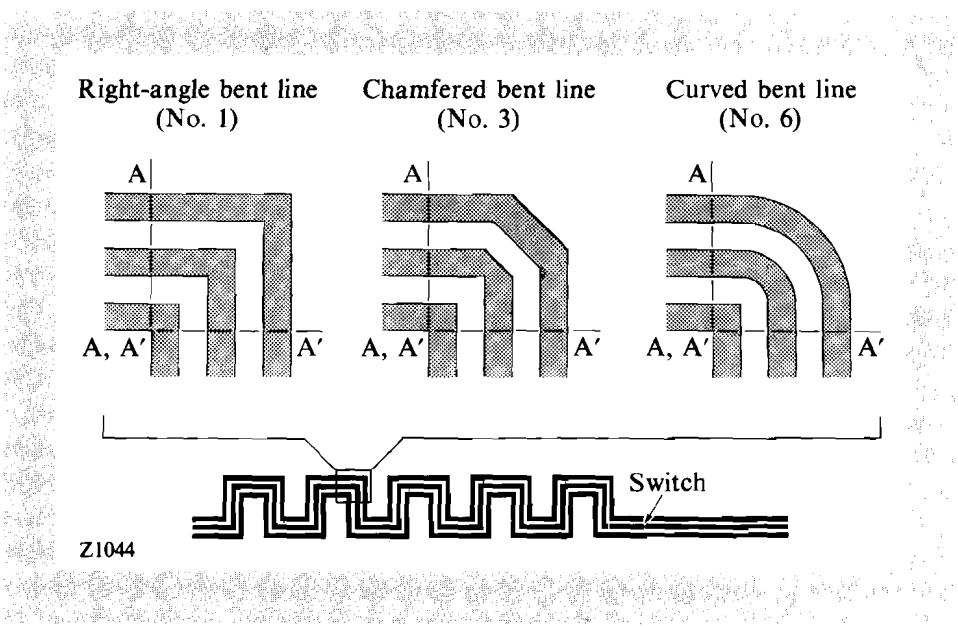

Fig. 47.22
Geometries of the bent CPW's studied in this work.

The measurements were performed with the aid of an electro-optic sampling system, similar to that described in Ref. 10. The CPW's were biased with a 10-V peak-to-peak square wave at a frequency of 3.5 MHz and terminated by a 50 Ω load. A colliding pulse, mode-locked dye laser was used to provide two trains of ~100-fs optical pulses (λ = 620 nm) at 100-MHz repetition rate. The first train of pulses (excitation train) was directed, via a short piece of an optical fiber, to the photoconductive switch (see Fig. 47.22) and used to launch a step-like electrical transient in the CPW. The implementation of the fiber enabled us to speed up the beam-alignment procedure and substantially improved reproducibility of the measured electrical transients. The second (probing) beam was fed to a small, movable electro-optic $LiTaO_3$

crystal (so-called "finger tip"), which was used to probe propagating electrical waveforms at different points along the transmission line.[10]

Results

Figure 47.23 shows the measured step-like electrical transients as they propagate along the bent CPW No. 6. The waveform (a) shows the input signal, while the waveforms (b), (c), and (d) show the same signal after it propagated through 2, 4, and 10 bends, respectively. Only the rising parts of the transients are shown for better clarity. The transients of the type presented in Fig. 47.23 enabled us to precisely determine both the signal arrival time (taken as the midpoint of the transient) and the 10%–90% rise time. As expected, the transient's rise time became longer as it propagated along the line. At the same time we did not observe any significant attenuation of our signals.

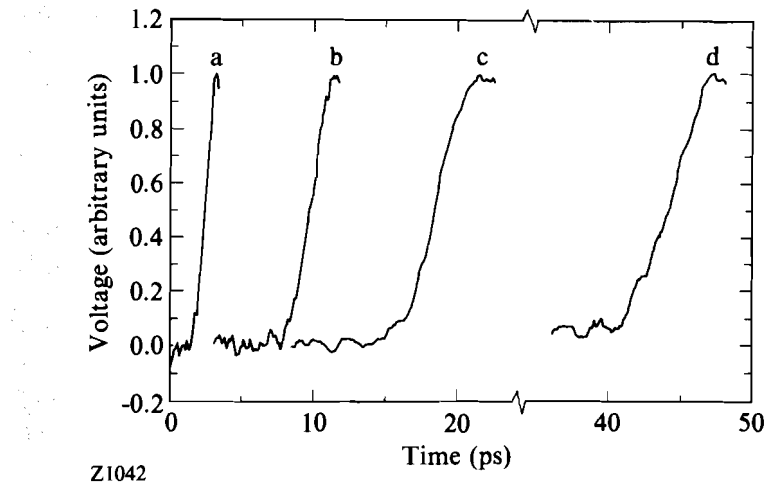

Fig. 47.23
Experimentally measured waveforms of the signal propagating on the curved-bent CPW (No. 6). (a) – the input transient; (b), (c), and (d) – the propagated signals after 2, 4, and 10 bends, respectively. The waveforms are normalized with respect to the amplitude of the input pulse, in order to eliminate spurious, measurement-to-measurement fluctuations.

The signal-propagation velocity v along the bent CPW's can be determined from a plot of propagation distance versus time as presented in Fig. 47.24. The propagation distance represents the full physical length of the CPW, defined as the path along the center of the CPW signal line. The bent CPW's exhibit the same propagation velocity as the straight CPW. Further, it is practically constant over the entire distance. All of the data points (including the ones for the CPW's not presented in Fig. 47.24) lie on the same straight line, which corresponds to the value of v given by the quasi-static approximation:

$$v = \frac{c}{\sqrt{\frac{\varepsilon_{air} + \varepsilon_{GaAs}}{2}}} = 0.38\, c\ , \qquad (1)$$

where $\varepsilon_{GaAs} = 12.9$, $\varepsilon_{air} = 1$, and c stands for the light velocity in vacuum. The result is in excellent agreement with Ref. 1 and suggests that, within our

frequency range, the propagation velocity (or equivalently signal dispersion) depends very weakly on the number of bends, or their shape.

The fact that the propagation distance represents the full physical length of the CPW supports an intuitive expectation that at the sub-THz frequency range the effect of propagation of the electrical signal along the bend must be fully taken into account. Thus, at these frequencies, one cannot follow the analysis given by Simons *et al.* (Ref. 8), where the bend (defined as the region of the CPW between A–A and A′–A′ cross sections in Fig. 47.22) was treated as the point discontinuity with a small, frequency-dependent length correction.

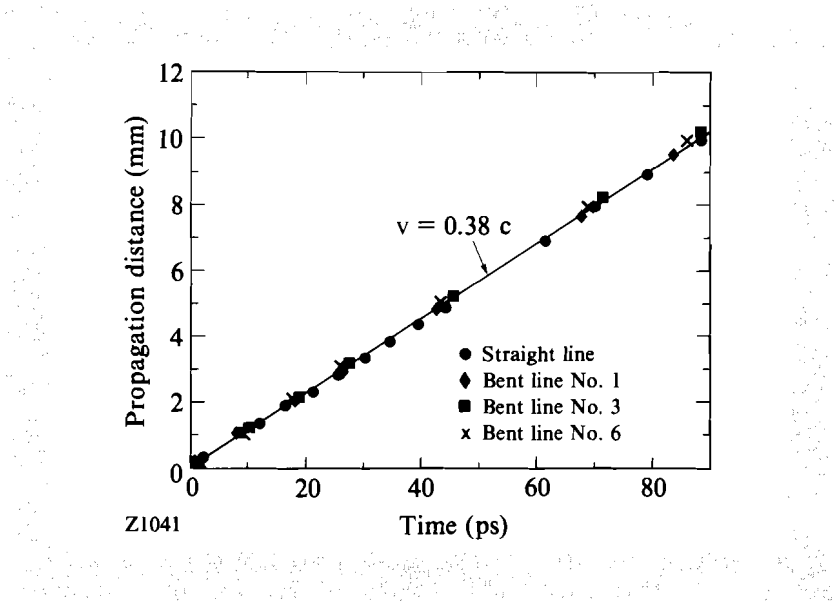

Fig. 47.24
Propagation distance versus time for the picosecond transients propagating on the straight and bent Au-on-GaAs CPW's. The straight line corresponds to the signal velocity within the quasi-static limit.

The variation of the rise times as the transients traveled along the bent and straight CPW's is shown in Fig. 47.25. As expected, the rise times were shortest for the straight line and they initially increased linearly with the propagation distance (see also Ref. 1). The bent CPW's exhibited considerably longer rise times in the initial propagation distance (0–3 mm), as compared to the straight line.We associate this effect with high-frequency reflections of the signal from the bends. For longer distances, the rise times continued to increase only for the right-angle-bent line (No. 1), while for the chamfered-bent line (No. 3) and the curved-bent line (No. 6), the values of the rise times leveled off to ~5 ps after 4 mm of propagation. At this frequency regime, the bent CPW's behaved almost like the straight line.

The observed difference in the rise times between the bent and the straight CPW's shows that the bend-induced distortion depends on the bend geometry and is significantly reduced for the smooth bends, which, apparently, cause less reflection. The distortion is also frequency dependent. However, for the curved- and chamfered-bent lines, it practically vanishes for transients longer than 5 ps. The previous observations show that high-frequency reflections from the bends are the leading mechanism of signal distortion in the bent CPW's operating in the sub-THz frequency range.

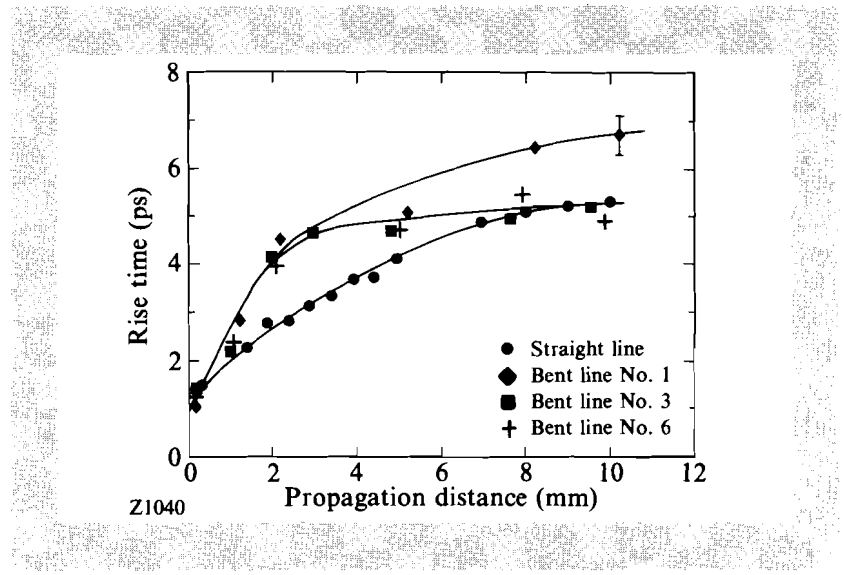

Fig. 47.25
Rise time versus the propagation distance comparison between the right-angle bent, smooth-bent, and straight CPW's. The error bar on the line No. 1 data point represents the maximal error of our measurements. The solid lines are only to guide the eye.

Conclusions

We have measured the propagation characteristics of the 20-bend CPW's over a distance of about 10 mm. Our results demonstrate that picosecond transients, having the bandwidth in excess of 100 GHz, can propagate over a large number of bends with a limited signal distortion. We have found that the physical length of the bent CPW must be taken into account in order to correctly evaluate the signal propagation velocity. Finally, we showed that smoothing of the bends considerably improves the very-high-frequency performance of the bent CPW's.

ACKNOWLEDGMENT

We would like to thank W. R. Donaldson, L. Golob, J. Variano, and N. Wakabayashi for their assistance. This work was partially supported by the Laser Fusion Feasibility Project at the Laboratory for Laser Energetics, which is sponsored by the New York State Energy Research and Development Authority and the University of Rochester.

REFERENCES

1. D. R. Dykaar, A. F. J. Levi, and M. Anzlowar, *Appl. Phys. Lett.* **57**, 1123 (1990).
2. M. Y. Frankel, S. Gupta, J. A. Valdmanis, and G. A. Mourou, "Tetrahertz attenuation and dispersion of coplanar transmission lines," submitted to *IEEE Trans. Microwave Theory Tech.*
3. D. S. Phatak, N. K. Das, and A. P. Defonzo, *IEEE Trans. Microwave Theory Tech.* **38**, 1719 (1990).
4. M. Riaziat, R. Majidi-Ahy, and I-J. Feng, *IEEE Trans. Microwave Theory Tech.* **38**, 245 (1990).
5. J. F. Whitaker, R. Sobolewski, D. R. Dykaar, T. Y. Hsiang, and G. A. Mourou, *IEEE Trans. Microwave Theory Tech.* **36**, 277 (1988), and references therein.
6. D. R. Dykaar, R. Sobolewski, J. M. Chwalek, J. F. Whitaker, T. Y. Hsiang, G. A. Mourou, D. K. Lathrop, S. E. Russek, and R. A. Buhrman, *Appl. Phys. Lett.* **52**, 1444 (1988).

7. M. C. Nuss *et al.*, *IEEE Electron Device Lett.* **11**, 200 (1990).

8. R. N. Simons *et al.*, *IEEE MTT-S International Microwave Symposium Digest*, 915 (1989).

9. R. Majidi-Ahy *et al.*, *IEEE Trans. Microwave Theory Tech.* **38**, 1986 (1990).

10. J. A. Valdmanis, *Electron. Lett.* **23**, 1308 (1987), and references therein.

2.B Angle-Resolved X-Ray Photoemission Study of the Surface Disordering of Pb(100)

A surface atom has a reduced number of nearest neighbors when compared to an atom in the bulk. This enhances the thermal vibrations of the surface atoms, often leading to surface disordering (or surface melting) below the bulk-melting temperature. The temperature-dependent disordering of surfaces can be studied using a variety of surface-sensitive techniques, such as ion shadowing and blocking,[1,2] low-energy electron diffraction (LEED),[3–6] x-ray scattering,[7] and x-ray photoelectron diffraction (XPD).[8] Results have conclusively shown that Pb(110) experiences surface disordering, and the temperatures for the various stages of surface disorder are well established.[1–8] Theoretical analysis has shown that the propensity for surface disorder with temperature depends on packing and is highest for open surfaces.[9] For example, Pb(111) is more densely packed than Pb(110) and is found to resist surface disordering up to the bulk-melting temperature (T_m = 600.7 K). Its temperature dependence has been almost entirely attributed to the Debye-Waller effect, i.e., the intensity attenuation of the diffraction peaks is exponential in temperature.[4] The Pb(100) surface is more closely packed than Pb(110) but less packed than Pb(111). We have found that Pb(100) experiences surface disordering but to a lesser degree than Pb(110).[10] Ion shadowing and blocking has been used to study the temperature-dependent disordering of Pb(100); approximately five disordered layers have been found on Pb(100) at about 600 K.[2] The rate of change of the disordered-layer thickness did not diverge as T_m was approached; thus, it has been suggested that Pb(100) is "on the verge" of surface melting.[2]

In our experiment we used XPD to study the dependence of the forward-scattered intensity of the [001] and [011] azimuths of Pb(100) on temperature. One of the most important characteristics of XPD is its strong forward scattering, i.e., the intensity is enhanced along inter-nuclear axes. The angular-intensity distribution can be used to characterize the degree of surface order.[11,12] For electron energies of several hundred electron volts, multiple scattering defocuses electrons emitted below approximately four atomic layers.[12] Hence, XPD is a highly surface-sensitive probe. We find that Pb(100) experiences an attenuation of the forward-scattered intensity that, above 550±11 K, cannot be explained solely by the Debye-Waller effect. Above 585±5 K, the rate of intensity attenuation increases and we attribute this to the growth of a surface-disordered layer. A slight anisotropy

is seen with the [011] azimuth experiencing a faster decay. By comparing our results along the [001] azimuth with previous experiments on Pb(110),[2,8] we estimate the disordered-layer thickness on Pb(100) to be 4–5 monolayers at 599±0.6 K.

Experiment and Data Analysis

The crystal was oriented within 0.75° of the Pb(100) surface as confirmed by Laue back reflection. The sample was cut with a fine-band saw to twice its final thickness, polished with silicon carbide grit paper, and finally chemically etched in a mixture of 80% glacial acetic acid and 20% hydrogen peroxide (30% in water). Prior to insertion in the ultrahigh vacuum (UHV) chamber, the sample was again chemically etched.

The sample was clipped to a resistively heated molybdenum base mounted on a five-axis manipulator. Two thermocouples monitored the temperature of the front and back surfaces of the sample. Temperature stability was better than ±0.6 K and the maximum temperature difference across the sample was 1 K. Data were taken to within 1.7±0.6 K of T_m. The thermocouples were calibrated to the freezing and boiling temperatures of water, and to the melting temperature of lead by melting the sample *in situ* at the conclusion of the experiment.

Before data acquisition, the sample was cleaned with argon-ion bombardment and annealed to approximately 2 K below T_m until an atomically clean surface was obtained. Oxygen and carbon levels were checked throughout the experiment via x-ray photoelectron spectroscopy (XPS) of the 1s transition for both elements. Auger electron spectroscopy was occasionally used to confirm the XPS results. A Mg Kα x-ray source (E = 1253.6 eV), at 28.8° from the surface normal, provided the incident radiation. The binding energy of the $4f_{7/2}$ core-level photoelectrons is 136.6 eV; therefore, 1117.0-eV electrons were emitted from the lead sample. The scattered electron intensity was detected with a hemispherical energy analyzer mounted on a two-axis goniometer. The resolution of the analyzer as determined by LEED is 1.6° FWHM. The base pressure of the UHV system is $<1 \times 10^{-10}$ Torr. The actual pressure during the experiment was higher because of argon-ion bombardment, the x-ray source, and heating of the sample. Sample orientation was checked with reflection high-energy electron diffraction and LEED. Intensities were recorded at angular steps of 1°.

Electrons with an energy of 1117.0 eV have an estimated inelastic mean-free path λ_{in} of 24 Å in lead.[13–15] This corresponds to a maximum escape depth of 10 monolayers for $\theta = 0°$ and 3 monolayers for $\theta = 72°$, where θ is the angle measured from the surface normal. However, multiple scattering events effectively reduce λ_{in} and must be included to provide accurate predictions.[16] Unfortunately, such calculations are complicated and therefore rarely incorporated in quantitative analysis. Recently, an effective electron mean-free path has been introduced that is affected by both the elastic and inelastic mean-free paths; multiple scattering can be partially accounted for in a single scattering calculation by substituting λ_{eff} for λ_{in},

where $0.5\,\lambda_{in} \leq \lambda_{eff} \leq 0.7\,\lambda_{in}$.[17] The possible dependence of λ_{eff} on crystal direction is still unaccounted for.

Forward-scattered peaks are expected to be visible at 0°, 18.4°, 45°, and 71.6° for the [001] azimuth, and 0°, 19.5°, 35.3°, and 54.7° for the [011] azimuth for a nonrelaxed (100) surface. We analyzed all eight of these peaks. In our polar scans, forward-scattered peaks appear within 1° of these expected values, except for the peak at 71.6° that appears within 2°. Discrepancies may arise from a small error in the spectrometer step size (within ±0.6% of the actual setting), interference effects, multilayer relaxation, and increased refraction for large θ angles.[12] However, multilayer relaxation and refraction effects are ruled out for the peak predicted at 71.6° since both would result in a change opposite to what is observed.[18] In addition, smaller peaks are observed at approximately 32° and 58° for [001] and 68° for [011]. These are due to first-order constructive interference at an off-axis angle, which results when the phase difference between the two paths is 2π.[12]

Our data acquisition was performed in the following manner. Polar scans were taken at 1117.0 eV and at two other energies (1133.6 eV and 1093.6 eV) for which no lead peaks are seen. The latter two polar scans were used to interpolate the background at 1117.0 eV for each value of θ. The background was then subtracted from the raw intensity data. This was completed during data acquisition and we refer to the resulting polar scans as as-acquired data. Further analysis was accomplished as follows. Nonforward-scattered electrons were accounted for by fitting a polynomial to the highest temperature data for each azimuth after the remaining forward scattering was removed. At such high temperatures, the forward-scattered peaks are weak because of surface disordering. The instrumental response was determined from a polar scan at 1133.6 eV that was fit to a polynomial. The data correction was accomplished as follows:

$$I_{corr}(\theta,T) = \frac{I(\theta,T)-I_{bkgd}(\theta,T)}{I_{ir}(\theta,T)}, \qquad (1)$$

where $I(\theta,T)$, $I_{bkgd}(\theta,T)$, and $I_{ir}(\theta,T)$ are the as-acquired data, nonforward-scattered background, and instrumental response given in Fig. 47.26(a), and $I_{corr}(\theta,T)$ is the corrected data shown in Fig. 47.26(b) for the [001] azimuth of Pb(100) at $T = 326\pm0.6$ K. θ is the angle from the surface normal and T is the temperature.

The temperature dependence of the intensity of the forward-scattered peaks $I_{corr}(\theta,T)$ for a given angle can be presented as a plot of $\ln[I_{corr}(\theta,T)]$ versus temperature. Such plots are shown for the [001] azimuth of Pb(100) in Fig. 47.27. The result is a linear dependence up to a particular temperature, which we have found to be 550±11 K for Pb(100), after which $\ln[I_{corr}(\theta,T)]$ diverges from linear behavior at an increasing rate. The line that best fits the data in the linear region is determined using the method of least squares; the number of data points included in the fit is chosen to maximize the statistical correlation coefficient between the line fit and the data. The linear

region, for which the intensity attenuation is exponential in temperature, is attributed to the Debye-Waller effect. At temperatures above 550±11 K, additional phenomena are necessary to describe the observed behavior.

Surface Disordering

The effects of a surface-disordered layer on the forward-scattered intensity are now considered. The intensity is exponentially attenuated with an exponent proportional to $l/\lambda_{eff}\cos\theta$ where l is the thickness of the disordered layer.[8] It has been shown that the disordered layer grows as a function of temperature according to the relation

$$l \sim \ln\left[(T_m - T_o)/(T_m - T)\right], \tag{2}$$

where T_o is the characteristic temperature for the onset of surface disorder.[1,3,8,19] This behavior is expected for a three-dimensional system governed by short-range atomic interactions; such is the case for metals.[2,20] If the disordered-layer thickness exceeds the range of these interactions, long-range forces become important and the disorder grows as a power law.[2] Given the exponential attenuation described above, as well as Eq. (2), the normalized intensity is expected to have the following form:[4,8]

$$I_{corr}(\theta,T)/I_{DW}(\theta,T) = \left[(T_m - T_o)/(T_m - T)\right]^r, \tag{3}$$

where $I_{DW}(\theta,T)$ is the Debye-Waller exponential function obtained from line fits such as in Fig. 47.27 and r is a constant that depends on λ_{eff} and θ.

We account for the Debye-Waller attenuation by dividing $I_{corr}(\theta,T)$ by $I_{DW}(\theta,T)$. In Fig. 47.28, $\ln[I_{corr}(\theta,T)/I_{DW}(\theta,T)]$ is plotted versus $\ln(T_m - T)$. The horizontal region where $\ln[I_{corr}(\theta,T)/I_{DW}(\theta,T)] = 0$ represents Debye-Waller behavior, and the linear region for high temperatures indicates logarithmic growth of the disordered layer. The intermediate temperature region shows a slow intensity attenuation in excess of that predicted by Debye-Waller. We attribute this behavior to partial disordering of the first atomic layer. We interpret the steep linear region at higher temperatures as the spread of disorder to deeper atomic layers. If this line fit is extrapolated to the temperature axis, we find T_o = 585±5 K for the [001] and [011] azimuths. A slight anisotropy is observed; [011] experiences a more rapid decrease in intensity above T_o. Consideration of the solid-liquid interface provides an explanation for the observed anisotropy.[3] The interfacial free energy is lowest in the direction in which the atomic spacing of the solid is closest to the atomic spacing of the liquid. For Pb(100) this occurs along the [011] azimuth. This is consistent with Pb(110) where the $[1\bar{1}0]$ azimuth disorders faster than [100].[3,4,6,8,21]

Using LEED, Prince *et al.*[3] have found T_o = 543±3 K for the [001] and $[1\bar{1}0]$ azimuths of Pb(110). In their experiment, the intensity disappeared into the background above approximately 575 K for $[1\bar{1}0]$ and approached the background for [001]. In an XPD experiment on Pb(110), Breuer and coworkers[8] have observed logarithmic growth of the disordered layer for a

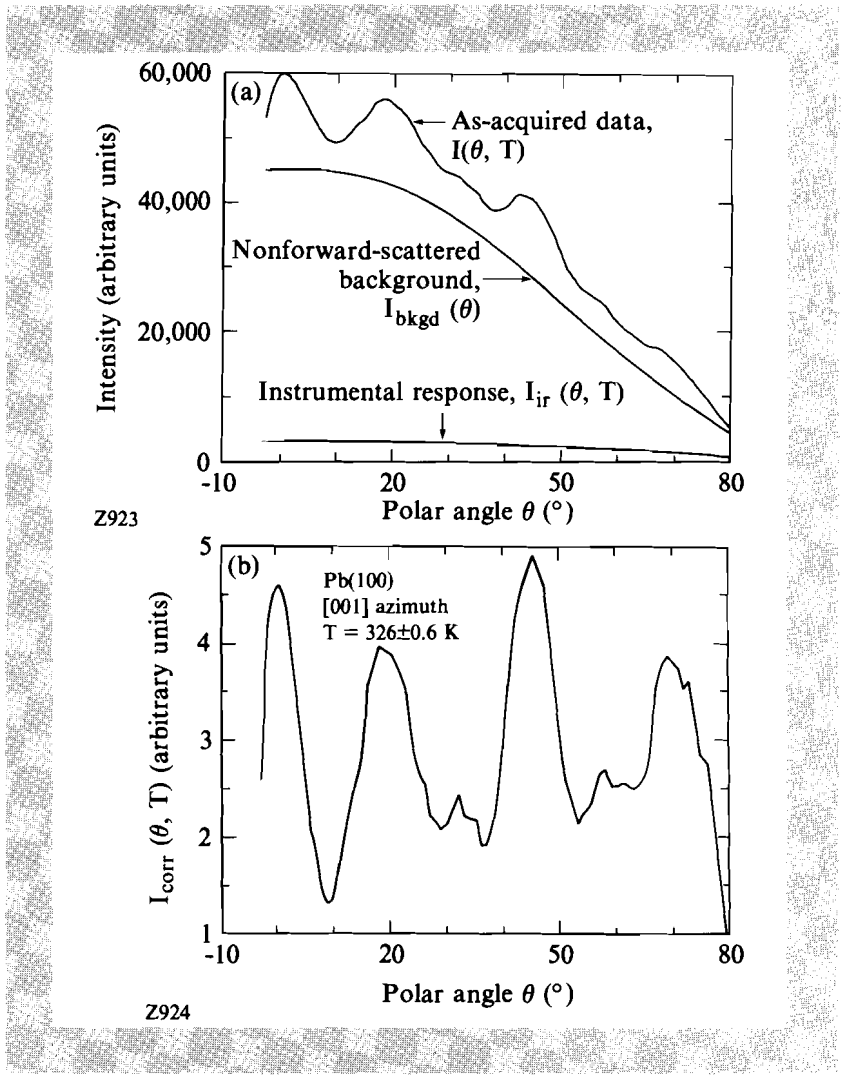

Fig. 47.26
Polar scans are shown for the [001] azimuth of Pb(100) at $T = 326 \pm 0.6$ K: (a) as-acquired data $I(\theta,T)$, nonforward-scattered background $I_{bkgd}(\theta,T)$, and instrumental response $I_{ir}(\theta,T)$. (b) The corrected forward-scattered intensity $I_{corr}(\theta,T)$, obtained using Eq. (1).

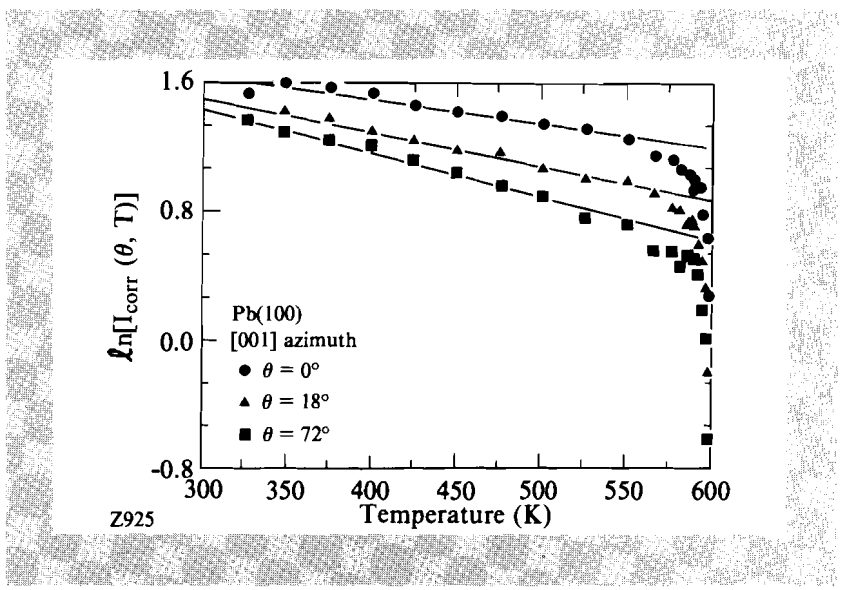

Fig. 47.27
The logarithm of the corrected forward-scattered peak intensity $\ln[I_{corr}(\theta,T)]$ is given as a function of temperature for various angles along the [001] azimuth. The linear region at low temperatures is attributed to the Debye-Waller effect. Deviation from Debye-Waller behavior is seen above 550±11 K.

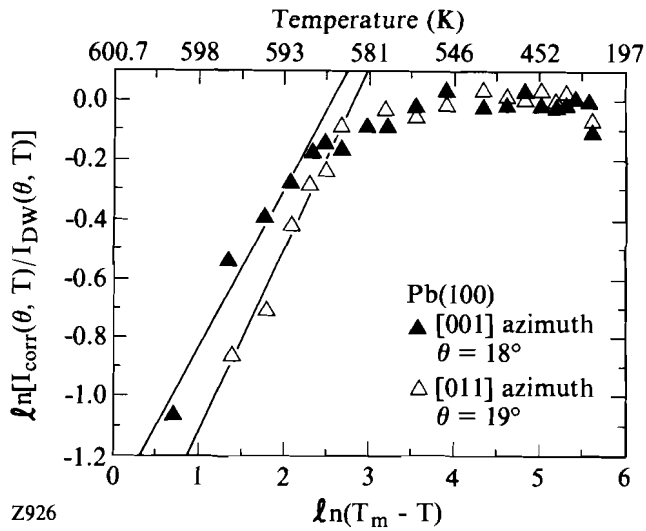

Fig. 47.28
The logarithm of the corrected forward-scattered peak intensity normalized to the Debye-Waller fit $\ln[I_{corr}(\theta,T)/I_{DW}(\theta,T)]$ is plotted versus $\ln(T_m-T)$. The line fit for temperatures above 585±5 K indicates that the disordered layer experiences logarithmic growth. Some anisotropy is seen; the [011] azimuth decays faster with temperature.

temperature region close to T_m. For a lower-temperature region they have reported the existence of another logarithmic growth law. They have concluded that $T_0 = 530 \pm 5$ K, and that the higher-temperature logarithmic-growth law dominated above 575 K. Temperatures for the onset of surface disorder and complete surface melting were found by Frenken *et al.*[1] to be about 545 K and 580 K, respectively, with ion shadowing and blocking.

In contrast to what has been observed on the Pb(110) surface, we find no evidence for a second logarithmic growth law for Pb(100). It is possible that such a growth law does not exist for Pb(100). This would indicate that Pb(100) experiences what is referred to as incomplete surface melting; that is, the rate of change of the thickness of the disordered layer does not diverge as T_m is approached. This is in contrast to complete surface melting where the disordered layer behaves increasingly like the bulk liquid and its thickness diverges as the temperature nears T_m.[21] Another possibility is that a second growth law exists for Pb(100) at temperatures closer to T_m than we have considered in our experiments.

We next consider the temperature dependence of the number of disordered layers for Pb(100). The temperature-dependent attenuation of the forward-scattered intensity peaks for Pb(110) as obtained by XPD[8] is related to the number of disordered layers on the surface as determined by Pluis *et al.*,[2] who used ion shadowing and blocking. Their data are compared to ours in Fig. 47.29. A deviation from Debye-Waller-like behavior is seen for Pb(110) around 500 K, and around 550 K for Pb(100). Two disordered layers have been found through analysis of the $[1\bar{1}0]$ azimuth, on Pb(110) at 550 K, 4 disordered layers at 587 K, and 8 disordered layers at 599.3 K.[2,8] From a comparison of the intensity attenuation of the [001] azimuth of Pb(100) with these results, we estimate the disordered-layer thickness on Pb(100) to be 2 layers at about 590 K, and 4–5 layers at about 599 K. This is in agreement with the previous results where close to 5 disordered layers were visible

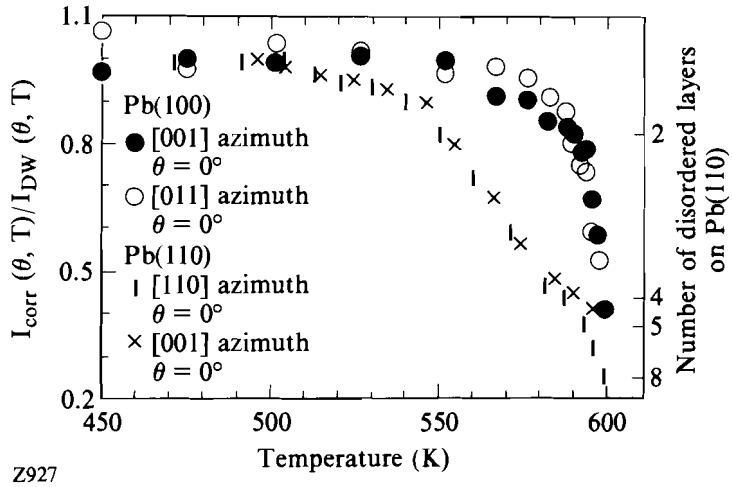

Fig. 47.29
The corrected forward-scattered peak intensities normalized to the Debye-Waller fit $I_{corr}(\theta,T)/I_{DW}(\theta,T)$ is plotted versus temperature for the [001] and [011] azimuths of Pb(100) for $\theta = 0°$. Normalized data for the [001] and [1$\bar{1}$0] azimuths of Pb(110) are from Ref. 8. The number of disordered layers on Pb(110) as a function of temperature from Refs. 2 and 8 are compared to $I_{corr}(\theta,T)/I_{DW}(\theta,T)$ to predict the number of disordered layers on Pb(100).

around 600 K for Pb(100).[2] The forward-scattered peak at 72° for the [001] azimuth of Pb(100) nearly disappears at 599 K, although not completely. Thus, slight order must still exist in the first 3 monolayers at 599 K (3 monolayers is the upper limit of the escape depth at 72°).

The thickness of the disordered layer can also be estimated by considering the attenuation of the forward-scattered peaks by elastic and inelastic scattering. These peaks are assumed to decay exponentially with the disordered-layer thickness:

$$\ln\left[I_{corr}(\theta,T)/I_{DW}(\theta,T)\right] = -l/\lambda_{eff}\cos\theta. \quad (4)$$

For the [001] azimuth of Pb(100) at 599±0.6 K and $\theta = 0°$, 4.5 to 6.3 disordered layers are predicted for $0.5\,\lambda_{in} \le \lambda_{eff} \le 0.7\,\lambda_{in}$.[17]

Conclusion

The [001] and [011] azimuths of Pb(100) exhibit surface disorder below the bulk-melting temperature, although the surface-melting process appears to be incomplete. Intensity attenuation can no longer be attributed to the Debye-Waller effect above 550±11 K. The characteristic temperature for the onset of surface disorder T_o is 585±5 K for both the [001] and [011] azimuths. A slight anisotropy is exhibited; the [011] has a more rapid intensity attenuation for temperatures above T_o. Comparison of our data for the [001] azimuth to previous work suggests that approximately 4–5 disordered atomic layers are present on the Pb(100) surface at 599±0.6 K.

ACKNOWLEDGMENT

This work was supported by the U. S. Department of Energy under contract No. DE-FG02-88ER45376. Additional support was provided by the National Science Foundation under contract No. DMR-8913880 as well as the Laser Fusion Feasibility Project at the Laboratory for Laser Energetics, which is sponsored by the New York State Energy Research and Development Authority and the University of Rochester. We gratefully acknowledge a research fellowship from the Alfred P. Sloan Foundation.

REFERENCES

1. J. W. M. Frenken and J. F. van der Veen, *Phys. Rev. Lett.* **54**, 134 (1985); J. W. M. Frenken, P. M. J. Maree, and J. F. van der Veen, *Phys. Rev. B* **34**, 7506 (1986).
2. B. Pluis *et al.*, *Phys. Rev. Lett.* **59**, 2678 (1987); B. Pluis *et al.*, *Phys. Rev. B* **40**, 1353 (1989); B. Pluis, Ph. D. thesis: *Surface-Induced Melting of Lead*, University of Leiden (1990).
3. K. C. Prince, U. Breuer, and H. P. Bonzel, *Phys. Rev. Lett.* **60**, 1146 (1988).
4. U. Breuer *et al.*, *Surf. Sci.* **223**, 258 (1989).
5. H. N. Yang, T. M. Lu, and G. C. Wang, *Phys. Rev. Lett.* **63**, 1621 (1989).
6. A. Pavlovska, H. Steffen, and E. Bauer, *Surf. Sci.* **234**, 143 (1990).
7. P. H. Fuoss, L. J. Norton, and S. Brennan, *Phys. Rev. Lett.* **60**, 2046 (1988).
8. U. Breuer, O. Knauff, and H. P. Bonzel, *Phys. Rev. B* **41**, 10848 (1990); U. Breuer, O. Knauff, and H. P. Bonzel, *J. Vac. Sci. Technol. A* **8**, 2489 (1990).
9. A. Trayanov and E. Tosatti, *Phys. Rev. B* **38**, 6961 (1988).
10. E. A. Murphy, H. E. Elsayed-Ali, K. T. Park, J. Cao, and Y. Gao, *Phys. Rev. B* **43**, 12615 (1991).
11. W. F. Egelhoff, Jr., *Phys. Rev. Lett.* **59**, 559 (1987).
12. W. F. Egelhoff, Jr., *CRC Crit. Rev. Solid State & Mater. Sci.* **16**, 213 (1990).
13. M. P. Seah and W. A. Dench, *Surf. & Interface Anal.* **1**, 2 (1979).
14. P. Cadman and G. M. Gossedge, *J. Electron Spectrosc. & Relat. Phenom.* **18**, 161 (1980).
15. D. Chadwick, A. B. Christie, and M. A. Karolewski, *Surf. & Interface Anal.* **11**, 144 (1988).
16. S. Y. Tong, H. C. Poon, and D. R. Snider, *Phys. Rev. B* **32**, 2096 (1985).
17. H. P. Bonzel, U. Breuer, and O. Knauff, *Surf. Sci.* **237**, L398 (1990).
18. R. F. Lin, Y. S. Li, F. Jona, and P. M. Marcus, *Phys. Rev. B* **42**, 1150 (1990).
19. R. Lipowsky, *Ferroelectrics* **73**, 69 (1987).
20. J. F. van der Veen, B. Pluis, and A. W. Denier van der Gon, *Chemistry and Physics of Solid Surfaces VII*, edited by R. Vanselow and R. Howe (Springer-Verlag, Berlin 1988), pp. 455–490.
21. R. Lipowsky *et al.*, *Phys. Rev. Lett.* **62**, 913 (1989).

Section 3
NATIONAL LASER USERS FACILITY NEWS

NLUF activity during the third quarter of FY91 included Thomson-scattering experiments by **K. Mizuno**; an investigation of how to manufacture targets filled with multiple gasses for **J. Moreno** and **C. Hooper**, and a review of proposals for FY92. These activities used the GDL laser facility, required support from the LLE target fabrication group, and used LLE facilities for the NLUF steering committee meeting.

Experiments by K. Mizuno of the Plasma Physics Research Center are in support of **J. De Groot's** (University of California, Davis) NLUF research effort. This work has developed a multichannel detector to measure Thomson scattering from laser-produced plasmas. The GDL laser is used to generate a hot, dense plasma and a second laser is used to probe this plasma. The probe laser for these measurements is a frequency-quadrupled Nd:YLF laser synchronized to GDL. The Thomson-scattered probe radiation is used to study the density profile of the plasma near the critical surface for the incident GDL beam. The first set of experiments was used to check out the new multichannel detector and to determine how difficult it would be to set up the experiment. Work will continue as instrumentation is improved.

Two groups would like to field targets filled with a mixture of D_2 gas plus a noble gas for their NLUF experiments. They are **H. Griem's** group at the University of Maryland and C. Hooper's group at the University of Florida. J. Moreno is leading the experiments for H. Griem and plans to use targets

filled with a mixture of D_2 and Ne to study the atomics physics of compressed cores. The primary diagnostic will be time-dependent measurements of the Ne emission in the XUV and x-ray parts of the spectrum. C. Hooper is continuing to study the properties of hot, dense matter by doing high-resolution temporal and spectral measurements of x rays. He plans to use targets filled with mixtures of D_2 and Ar and to measure the line shapes of the *k*-shell Ar emission. Both of these experiments require the availability of multi-gas targets. The LLE target fabrication group has been studying techniques needed to manufacture these targets.

The NLUF steering committee met on 14 June 1991 to review the seven proposals submitted to DOE for FY92. Details of the technical review will be discussed after the steering committee has approved the minutes of the meeting.

ACKNOWLEDGMENT

This work was supported by the U.S. Department of Energy Office of Inertial Confinement Fusion under agreement No. DE-FC03-85DP40200.

Section 4
LASER SYSTEM REPORT

4.A GDL Facility Report

There was a total of 378 GDL shots during the third quarter of FY91. Most of the target shots were in support of NLUF users from the University of California, Davis and the University of Illinois. The laser system shots were required to realign the laser-amplifier chain and to optimize system performance. Synchronization of the probe laser to the GDL laser was also checked.

The shot summary for the GDL laser this quarter is as follows:

Laser system		238
Calibration		18
Target		122
	TOTAL	378

ACKNOWLEDGMENT

This work was supported by the U.S. Department of Energy Office of Inertial Confinement Fusion under agreement No. DE-FC03-85DP40200 and by the Laser Fusion Feasibility Project at the Laboratory for Laser Energetics, which is sponsored by the New York State Energy Research and Development Authority and the University of Rochester.

4.B OMEGA Facility Report

The OMEGA laser was used for a series of flat-target, long-scale-length plasma experiments at the beginning of the third quarter of FY91. These experiments required OMEGA to be reconfigured, including changes to the timing of several beams relative to each other, and the redirection of one of the OMEGA beams to enter the target chamber through a 12-inch equatorial port. The system has been reset for spherical-target experiments and system-wide maintenance has been performed.

The primary activity on OMEGA has been the installation of a pulse-shaping system on the driver line. This system replaces the oscillator when shaped pulses are required for target experiments. The system consists of a Coherent Optics Antares™ laser that drives two regenerative amplifiers. One amplifier is used to produce a long (1.1-ns FWHM) pulse and the second amplifier is used to amplify a short (50-ps FWHM) pulse that drives an optically triggered silicon switch. The silicon switch is used to control the voltage across a Pockels cell through which the long pulse is propagated. Thus the desired pulse shape is "carved" out of the long pulse. A series of spherical implosion experiments will be conducted when the installation of this apparatus has been completed.

The shot summary for OMEGA this quarter is as follows:

Software test		10
Driver		116
Laser		200
Target		54
	TOTAL	380

ACKNOWLEDGMENT

This work was supported by the U.S. Department of Energy Office of Inertial Confinement Fusion under agreement No. DE-FC03-85DP40200 and by the Laser Fusion Feasibility Project at the Laboratory for Laser Energetics, which is sponsored by the New York State Energy Research and Development Authority and the University of Rochester.

PUBLICATIONS AND CONFERENCE PRESENTATIONS

Publications

S. Augst, D. D. Meyerhofer, D. Strickland, and S. L. Chin, "Laser Ionization of Noble Gases by Coulomb-Barrier Suppression," *J. Opt. Soc. Am. B* **8**, 858–867 (1991).

D. K. Bradley, T. Boehly, D. L. Brown, J. Delettrez, W. Seka, and D. Smith, "Early-Time 'Shine-Through' in Laser Irradiated Targets," in *Laser Interaction and Related Plasma Phenomena*, edited by H. Hora and G. H. Miley (Plenum Press, New York, 1991), Vol. 9, pp. 323–334.

Y.-H. Chuang, D. D. Meyerhofer, S. Augst, H. Chen, J. Peatross, and S. Uchida, "Suppression of the Pedestal in a Chirped-Pulse-Amplification Laser," *J. Opt. Soc. Am. B* **8**, 1226–1235 (1991).

W. R. Donaldson and L. E. Kingsley, "Optical Probing of Field-Dependent Effects in GaAs Photoconductive Switches," in *Optically Activated Switching* (SPIE, Bellingham, WA, 1990), Vol. 1378, pp. 226–236.

P. A. Jaanimagi, C. Hestdalen, J. Kelly, and W. Seka, "High Precision Measurements of the 24-Beam UV OMEGA Laser," in *19th International Congress on High-Speed Photography and Photonics* (SPIE, Bellingham, WA, 1990), Vol. 1358, pp. 337–343.

R. L. McCrory and C. P. Verdon, "Inertial Confinement Fusion: Computer Simulation," in *Computer Applications of Plasma Science and Engineering*, edited by A. Drobot (Springer-Verlag, New York, 1991), pp. 627–631.

E. A. Murphy, H. E. Elsayed-Ali, K. T. Park, J. Cao, and Y. Gao, "Angle-Resolved X-Ray-Photoemission Study of the Surface Disordering of Pb(100)," *Phys. Rev. B* **43**, 12,615–12,618 (1991).

N. Sampat, "The RS-170 Video Standard and Scientific Imaging: The Problems," *Advanced Imaging* **6**, 40–43 (1991).

W. Seka, D. Golding, B. Klein, R. J. Lanzafame, and D. Rogers, "Laser Energy Repartition Inside Metal, Sapphire, and Quartz Surgical Laser Tips," in *Application of Optical Engineering CAN-AM Eastern '90* (SPIE, Bellingham, WA, 1990), Vol. 1398, pp. 162–169.

L. J. Shaw-Klein, S. J. Burns, and S. D. Jacobs, "Thermal Conductivity of Aluminum Nitride Thin Films," in *Electronic Packaging Materials Science V*, edited by E. D. Lillie, P. S. Ho, R. Jaccodine, and K. Jackson (Materials Research Society, Pittsburgh, PA, 1991), Vol. 203, pp. 235–240.

J. M. Soures, "Progress in Inertial Fusion (Remarks of John M. Soures)," *J. Fusion Energy* **8**, 59–62 (1989).

C. J. Twomey and S.-H. Chen, "Solid Polymers Doped with Rare Earth Metal Salts I. Complex Formation and Morphology in Neodymium Chloride-Poly(Ethylene Oxide) System," *J. Polym. Sci., Polym. Phys. Ed.* **29**, 859–865 (1991).

C. P. Verdon, R. L. McCrory, R. Epstein, H. M. Van Horn, and M. P. Savedoff, "Some Effects of the UV Radiation from White Dwarfs on the Accretion of Interstellar Hydrogen," in the *Proceedings of the 7th European Workshop on White Dwarfs*, edited by G. Vauclair and E. Sion (Kluwer Academic Publishers, The Netherlands, 1991), pp. 295–304.

Forthcoming Publications

S. Alexandrou, R. Sobolewski, H. Nakano, B. C. Tousley, and T. Y. Hsiang, "Picosecond Characterization of Bent Coplanar Waveguides," to be published in *IEEE Microwave and Guided Wave Letters*.

S. Augst, D. D. Meyerhofer, J. Peatross, and C. I. Moore, "Spatial Distribution of High-Order Harmonics Generated in the Tunneling Regime," to be published in the *Proceedings of the Topical Meeting on Short-Wavelength Coherent Radiation: Generation and Application*, Monterey, CA, 8–10 April 1991.

H. Chen, Y.-H. Chuang, J. A. Delettrez, S. Uchida, and D. D. Meyerhofer, "Study of X-Ray Emission from Picosecond Laser-Plasma Interaction," to be published in the *Proceedings of the SPIE's OE/LASE '91 Symposium*, Los Angeles, CA, 20–25 January 1991.

P.-C. Cheng, H. Kim, and T. H. Lin, "The Study of Silica Deposition in the Leaf Blade of Zea mays L. by X-Ray Contact Microradiography and Confocal Microscopy," to be published in *X-Ray Microscopy III*, edited by A. Michette *et al.* (Springer-Verlag, New York).

Y.-H. Chuang, J. Peatross, and D. D. Meyerhofer, "Modeling the Pedestal in a Chirped-Pulse-Amplification Laser," to be published in the *Proceedings of the SPIE's OE/LASE '91 Symposium*, Los Angeles, CA, 20–25 January 1991.

Y.-H. Chuang, L. Zheng, and D. D. Meyerhofer, "Propagation of Light Pulses in a Chirped-Pulse-Amplification Laser," to be published in *IEEE Journal of Quantum Electronics*.

J. Delettrez, R. Epstein, D. K. Bradley, P. A. Jaanimagi, R. C. Mancini, and C. F. Hooper, "Hydrodynamic Simulations, with Non-LTE Atomic Physics, of High-Density Implosions of Argon-Filled Polymer Shell Targets," to be published in the *Proceedings of the 1990 International Workshop on Radiative Properties of Hot Dense Matter*, Sarasota, FL, 22–26 October 1990.

W. R. Donaldson, "Optical Probing of Field Dependent Effects in GaAs Photoconductive Switches," to be published in the *Proceedings of the IEEE 8th Pulsed Power Conference*, San Diego, CA, 17–19 June 1991.

H. E. Elsayed-Ali, J. W. Herman, and K. K. Lo, "Picosecond Time-Resolved Electron Diffraction Studies of Laser Heated Metals," to be published in the *Proceedings of the International Conference on Lasers '90*, McLean, VA, 10–14 December 1990 (invited paper).

E. M. Epperlein, "Electron Kinetics in Laser-Driven Inertial Confinement Fusion," to be published in the *Proceedings of the Topical Conference on Research Trends in Nonlinear and Relativistic Effects in Plasmas*, La Jolla, CA, 5–8 February 1990.

E. M. Epperlein, "Laser Filamentation in Plasmas," to be published in the *Proceedings of Topical Conference on Research Trends in Inertial Confinement Fusion*, La Jolla, CA, 4–6 February 1991.

E. M. Epperlein, "Kinetic Simulations of Laser Filamentation in Plasmas," to be published in *Physics of Fluids*.

E. M. Epperlein and R. W. Short, "A Practical Nonlocal Model for Electron Heat Transport in Laser Plasmas," to be published in *Physics of Fluids*.

R. Epstein and B. Yaakobi, "The Effect of Photoelectric Fluorescence on the Formation of X-Ray Absorption Lines in Laser-Plasma Experiments," to be published in *Physical Review A*.

P. M. Fauchet, "Applied Optical Diagnostics of Semiconductors," to be published in *IEEE Journal of Quantum Electronics* (invited paper).

P. M. Fauchet, D. A. Young, W. L. Nighan, Jr., and C. M. Fortmann, "Picosecond Carrier Dynamics in a-$Si_{0.5}Ge_{0.5}$:H Measured with a Free Electron Laser," to be published in *IEEE Journal of Quantum Electronics*.

T. Gong and P. M. Fauchet, "Femtosecond Refractive and Absorptive Nonlinearities Due to Real Carriers in GaAs," to be published in the *Proceedings of the IEEE/Lasers and Electro-Optics Society of America. Picosecond Electronics and Optoelectronics Conference*, Salt Lake City, UT, 13–15 March 1991.

T. Gong, P. Mertz, W. L. Nighan, Jr., and P. M. Fauchet, "Femtosecond Carrier Induced Changes of Refractive Index in GaAs," to be published in *Applied Physics*.

T. Gong, J. F. Young, P. J. Kelly, and P. M. Fauchet, "Femtosecond Gain Dynamics Due to Initial Thermalization of Hot Carriers Injected at 2 eV in GaAs," to be published in *Physical Review B*.

A. Honig, N. Alexander, Q. Fan, R. Q. Gram, and H. Kim, "Absence of Molecular Deuterium Dissociation During Room-Temperature Permeation into Polystyrene ICF Target Shells," to be published in the *Journal of Vacuum Science and Technology A*.

Conference Presentations

S. Augst, D. D. Meyerhofer, J. Peatross, and C. I. Moore, "Spatial Distribution of High-Order Harmonics Generated in the Tunneling Regime," presented at the Topical Meeting on Short-Wavelength Coherent Radiation: Generation and Application, Monterey, CA, 8–10 April 1991.

The following presentations were made at the 21st Annual Anomalous Absorption Conference, Banff, Alberta, Canada, 14–19 April 1991:

R. E. Bahr, W. D. Seka, R. S. Craxton, D. L. Brown, D. K. Bradley, and S. A. Letzring, "Characterization of Long-Scale-Length Plasmas on OMEGA."

D. K. Bradley, J. A. Delettrez, and C. P. Verdon, "Further Investigations of the Role of the Rayleigh-Taylor Instability in Burnthrough Measurements."

X. D. Cao and C. J. McKinstrie, "The Optimization of Sum-Frequency Generation."

H. Chen, Y.-H. Chuang, J. A. Delettrez, P. A. Jaanimagi, S. Uchida, B. Yaakobi, and D. D. Meyerhofer, "Studies of X-Ray Emission From 1 ps Laser-Plasma Interactions."

R. S. Craxton, W. D. Seka, and D. L. Brown, "Long-Scale-Length Plasmas for the OMEGA Upgrade."

J. A. Delettrez, P. Audebert, and D. D. Meyerhofer, "Modeling of Resonance Absorption in Hydrodynamic Simulations of 1-ps Laser Pulse Interaction."

E. M. Epperlein, "Fokker-Planck Simulations of Laser Filamentation in Plasmas."

R. Epstein, J. A. Delettrez, D. K. Bradley, P. A. Jaanimagi, R. C. Mancini, and C. F. Hooper, "Simulation of Absorption Spectra from High-Density Implosions of Argon Filled Polymer Shell Targets."

F. J. Marshall, J. A Delettrez, R. S. Craxton, and C. P. Verdon, "Space-Resolved Spectroscopy of OMEGA CD Target Implosions."

C. J. McKinstrie, G. G. Luther, and M. V. Goldman, "Three-Dimensional Instabilities of Counterpropagating Light Waves."

D. D. Meyerhofer, "The Interaction of High Intensity Lasers with Short Scale-Length Plasmas" (invited talk).

W. D. Seka, A. Simon, R. W. Short, R. E. Bahr, R. S. Craxton, D. L. Brown, D. D. Meyerhofer, and L. Zheng, "Nonlinear Interaction Processes in Long-Scale-Length Plasma Experiments on OMEGA."

R. W. Short, "The Filamentation Instability in the Presence of More than One Pump Wave."

S. Uchida, H. Chen, Y.-H. Chuang, J. A. Delettrez, and D. D. Meyerhofer, "Characteristics of Ion Emission From 1 ps Laser Pulse Interactions with Short Scale-Length Plasmas."

M. Yu and C. J. McKinstrie, "The Role of Ion Momentum in Stimulated Raman Scattering."

The following presentations were made at the IAEA Technical Committee Meeting on Drivers for Inertial Confinement Fusion, Osaka, Japan, 15–19 April 1991:

J. H. Kelly, M. J. Shoup III, M. M. Tedrow, C. D. Kiikka, T. J. Kessler, S. A. Kumpan, A. W. Schmid, M. D. Skeldon, and D. J. Smith, "The 30 kJ OMEGA Upgrade at the University of Rochester, a Flexible, High-Performance Nd:Glass Driver."

R. L. McCrory, J. M. Soures, J. P. Knauer, S. A. Letzring, F. J. Marshall, S. Skupsky, W. D. Seka, C. P. Verdon, D. K. Bradley, R. S. Craxton, J. A. Delettrez, R. Epstein, P. A. Jaanimagi, R. L. Keck, T. J. Kessler, H. Kim, R. L. Kremens, P. W. McKenty, R. W. Short, and B. Yaakobi, "Short-Wavelength-Laser Requirements for Direct-Drive Ignition and Gain."

J. M. Soures, R. L. McCrory, T. R. Boehly, R. S. Craxton, S. D. Jacobs, J. H. Kelly, T. J. Kessler, J. P. Knauer, R. L. Kremens, S. A. Kumpan, S. A. Letzring, W. D. Seka, R. W. Short, M. D. Skeldon, S. Skupsky, and C. P. Verdon, "OMEGA Upgrade Laser for Direct-Drive Target Experiments."

D. Golding, W. Seka, and R. J. Lanzafame, "Interaction of CO_2 Laser Light with Plume Resulting from Tissue Ablation," presented at the American Society for Laser Medicine and Surgery, San Diego, CA, 29 April–1 May 1991.

The following presentations were made at CLEO '91 Conference, Baltimore, MD, 12–17 May 1991:

S. Alexandrou, R. Sobolewski, H. Nakano, B. C. Tousley, and T. Y. Hsiang, "Propagation of Picosecond Transients on Bent Coplanar Waveguides."

J. M. Soures, R. L. McCrory, D. Bradley, R. S. Craxton, J. Delettrez, H. Kim, P. Jaanimagi, T. Kessler, J. Knauer, R. Kremens, S. Letzring, F. Marshall, W. Seka, R. Short, S. Skupsky, C. Verdon, and B. Yaakobi, "Direct-Drive Laser Fusion Experiments Using Smoothing by Spectral Dispersion (SSD)" (invited paper).

The following presentations were made at the QELS '91 Conference, Baltimore, MD, 12–17 May 1991:

S. Augst, D. D. Meyerhofer, J. Peatross, and C. I. Moore, "Spatial Distribution of High Order Harmonics Generated with a Nd:Glass Laser."

H. E. Elsayed-Ali, T. Juhasz, X. H. Hu, and W. E. Bron, "Temperature Dependence of Femtosecond Thermoreflectivity of Thin Gold Films."

T. Gong and P. M. Fauchet, "Femtosecond Refractive and Absorptive Nonlinearities Due to Real Carriers in GaAs."

C. J. McKinstrie, G. G. Luther, and M. V. Goldman, "Three-Dimensional Instabilities of Counterpropagating Light Waves."

The following presentations were made at the IEEE 8th Pulsed Power Conference, San Diego, CA, 17–19 June 1991:

W. R. Donaldson, "Optical Probing of Field Dependent Effects in GaAs Photoconductive Switches."

W. Donaldson and L. Kingsley, "Electric-Field Profiles in GaAs Photoconductive Switches."

W. R. Donaldson, A. Kadin, P. Ballentine, and K. Kortkamp, "An Optically-Triggered, Superconducting, Opening Switch," presented at the SDIO Pulsed Power Workshop, Los Angeles, CA, 19–21 June 1991.

D. D. Meyerhofer, S. Augst, J. Peatross, and C. I. Moore, "Spatial Distribution of High Order Harmonics Generated with a ND:Glass Laser," presented at the Big Sky Workshop on Super-Intense Laser Atom Physics, Big Sky, Montana, 22–25 June 1991; and at the SPIE International Symposium on Optical Applied Science and Engineering, San Diego, CA, 21–26 July 1991 (invited talk).

ACKNOWLEDGMENT

The work described in this volume includes current research at the Laboratory for Laser Energetics, which is supported by New York State Energy Research and Development Authority, the University of Rochester, the U.S. Department of Energy Office of Inertial Confinement Fusion under agreement No. DE-FC03-85DP40200, and other agencies.

UNIVERSITY OF
ROCHESTER